Since January 2020 Elsevier has created a COVID-19 resource centre with free information in English and Mandarin on the novel coronavirus COVID-19. The COVID-19 resource centre is hosted on Elsevier Connect, the company's public news and information website.

Article

Cell Host & Microbe

Virological characteristics of the SARS-CoV-2 Omicron BA.2.75 variant

Graphical abstract

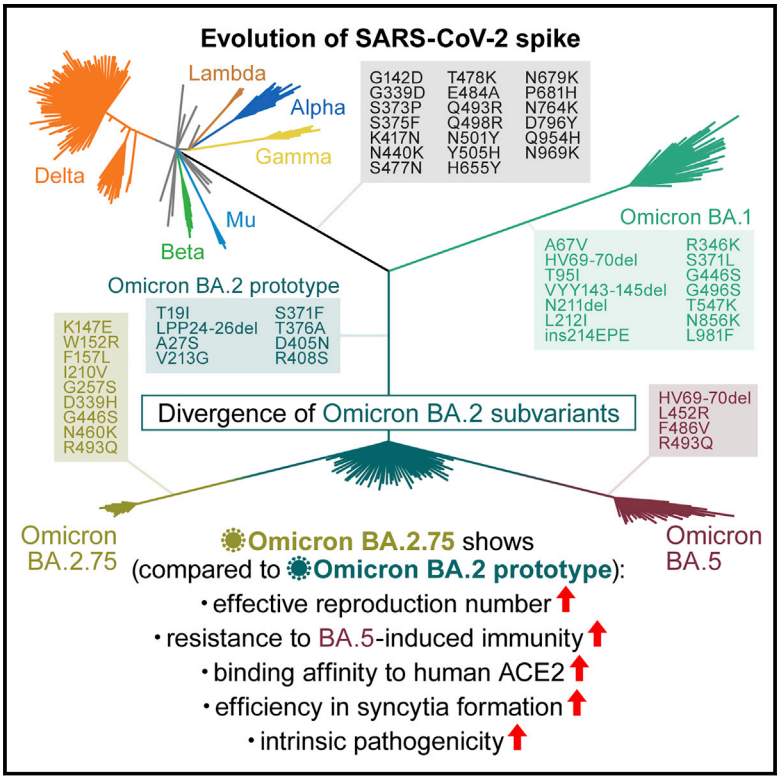

Highlights

- BA.2.75 is more transmissible than BA.5
- Immunogenicity of BA.2.75 spike is different from that of BA.2 and BA.5
- Compared with BA.2, BA.2.75 exhibits higher affinity to ACE2 and greater fusogenicity
- In infected hamsters, BA.2.75 exhibits greater pathogenicity than BA.2

Authors

Akatsuki Saito, Tomokazu Tamura, Jiri Zahradnik, ..., Terumasa Ikeda, Takasuke Fukuhara, Kei Sato

Correspondence

tanaka@med.hokudai.ac.jp (S.T.), ikedat@kumamoto-u.ac.jp (T.I.), fukut@pop.med.hokudai.ac.jp (T.F.), keisato@g.ecc.u-tokyo.ac.jp (K.S.)

In brief

Saito and G2P-Japan Consortium et al. elucidate the virological properties of the SARS-CoV-2 Omicron BA.2.75 variant. BA.2.75 is more transmissible than BA.5 and exhibits different antigenicity than BA.2 and BA.5. The BA.2.75 spike exhibits higher affinity to ACE2 and higher fusogenicity, and BA.2.75 is more pathogenic than BA.2 in hamsters.

Saito et al., 2022, Cell Host & Microbe *30*, 1–16
November 9, 2022
https://doi.org/10.1016/j.chom.2022.10.003

CellPress

Please cite this article in press as: Saito et al., Virological characteristics of the SARS-CoV-2 Omicron BA.2.75 variant, Cell Host & Microbe (2022), https://doi.org/10.1016/j.chom.2022.10.003

Cell Host & Microbe

CellPress
OPEN ACCESS

Article

Virological characteristics of the SARS-CoV-2 Omicron BA.2.75 variant

Akatsuki Saito,[1,2,3,40] Tomokazu Tamura,[4,40] Jiri Zahradnik,[5,6,40] Sayaka Deguchi,[7,40] Koshiro Tabata,[8,40] Yuki Anraku,[9,40] Izumi Kimura,[10,40] Jumpei Ito,[10,40] Daichi Yamasoba,[10,11,40] Hesham Nasser,[12,13] Mako Toyoda,[14] Kayoko Nagata,[15] Keiya Uriu,[10,16] Yusuke Kosugi,[10,16] Shigeru Fujita,[10,16] Maya Shofa,[1,2] MST Monira Begum,[12] Ryo Shimizu,[12] Yoshitaka Oda,[17] Rigel Suzuki,[4] Hayato Ito,[4] Naganori Nao,[18] Lei Wang,[17,19] Masumi Tsuda,[17,19] Kumiko Yoshimatsu,[20] Jin Kuramochi,[21,22] Shunsuke Kita,[9] Kaori Sasaki-Tabata,[23] Hideo Fukuhara,[24,25] Katsumi Maenaka,[9,24,25]

(Author list continued on next page)

[1]Department of Veterinary Science, Faculty of Agriculture, University of Miyazaki, Miyazaki, Japan
[2]Graduate School of Medicine and Veterinary Medicine, University of Miyazaki, Miyazaki, Japan
[3]Center for Animal Disease Control, University of Miyazaki, Miyazaki, Japan
[4]Department of Microbiology and Immunology, Faculty of Medicine, Hokkaido University, Sapporo, Japan
[5]Department of Biomolecular Sciences, Weizmann Institute of Science, Rehovot, Israel
[6]First Medical Faculty at Biocev, Charles University, Vestec, Prague, Czechia
[7]Center for iPS Cell Research and Application (CiRA), Kyoto University, Kyoto, Japan
[8]Division of Molecular Pathobiology, International Institute for Zoonosis Control, Hokkaido University, Sapporo, Japan
[9]Laboratory of Biomolecular Science and Center for Research and Education on Drug Discovery, Faculty of Pharmaceutical Sciences, Hokkaido University, Sapporo, Japan
[10]Division of Systems Virology, Department of Microbiology and Immunology, The Institute of Medical Science, The University of Tokyo, Tokyo, Japan
[11]Faculty of Medicine, Kobe University, Kobe, Japan
[12]Division of Molecular Virology and Genetics, Joint Research Center for Human Retrovirus infection, Kumamoto University, Kumamoto, Japan
[13]Department of Clinical Pathology, Faculty of Medicine, Suez Canal University, Ismailia, Egypt
[14]Division of Infection and immunity, Joint Research Center for Human Retrovirus infection, Kumamoto University, Kumamoto, Japan
[15]Department of Hematology and Oncology, Graduate School of Medicine, Kyoto University, Kyoto, Japan
[16]Graduate School of Medicine, The University of Tokyo, Tokyo, Japan
[17]Department of Cancer Pathology, Faculty of Medicine, Hokkaido University, Sapporo, Japan
[18]Division of International Research Promotion, International Institute for Zoonosis Control, Hokkaido University, Sapporo, Japan
[19]Institute for Chemical Reaction Design and Discovery (WPI-ICReDD), Hokkaido University, Sapporo, Japan

(Affiliations continued on next page)

SUMMARY

The SARS-CoV-2 Omicron BA.2.75 variant emerged in May 2022. BA.2.75 is a BA.2 descendant but is phylogenetically distinct from BA.5, the currently predominant BA.2 descendant. Here, we show that BA.2.75 has a greater effective reproduction number and different immunogenicity profile than BA.5. We determined the sensitivity of BA.2.75 to vaccinee and convalescent sera as well as a panel of clinically available antiviral drugs and antibodies. Antiviral drugs largely retained potency, but antibody sensitivity varied depending on several key BA.2.75-specific substitutions. The BA.2.75 spike exhibited a profoundly higher affinity for its human receptor, ACE2. Additionally, the fusogenicity, growth efficiency in human alveolar epithelial cells, and intrinsic pathogenicity in hamsters of BA.2.75 were greater than those of BA.2. Our multilevel investigations suggest that BA.2.75 acquired virological properties independent of BA.5, and the potential risk of BA.2.75 to global health is greater than that of BA.5.

INTRODUCTION

Newly emerging SARS-CoV-2 variants need to be carefully and rapidly assessed for a potential increase in their growth efficiency in the human population (i.e., relative effective reproduction number [R_e]), their evasion from antiviral immunity, and their pathogenicity. Resistance to antiviral humoral immunity can be mainly determined by substitutions in the spike (S) protein. For instance, Omicron BA.1 (Cao et al., 2021; Cele et al., 2021; Dejnirattisai et al., 2022; Garcia-Beltran et al., 2021; Liu et al., 2021;

Please cite this article in press as: Saito et al., Virological characteristics of the SARS-CoV-2 Omicron BA.2.75 variant, Cell Host & Microbe (2022), https://doi.org/10.1016/j.chom.2022.10.003

Yuki Yamamoto,[26] Tetsuharu Nagamoto,[26] Hiroyuki Asakura,[27] Mami Nagashima,[27] Kenji Sadamasu,[27] Kazuhisa Yoshimura,[27] Takamasa Ueno,[14] Gideon Schreiber,[5] Akifumi Takaori-Kondo,[15] The Genotype to Phenotype Japan (G2P-Japan) Consortium, Kotaro Shirakawa,[15] Hirofumi Sawa,[8,18,28] Takashi Irie,[29] Takao Hashiguchi,[30] Kazuo Takayama,[7,31] Keita Matsuno,[28,32,33] Shinya Tanaka,[17,19,*] Terumasa Ikeda,[12,*] Takasuke Fukuhara,[4,34,*] and Kei Sato[10,16,35,36,37,38,39,41,42,*]

[20]Institute for Genetic Medicine, Hokkaido University, Sapporo, Japan
[21]Interpark Kuramochi Clinic, Utsunomiya, Japan
[22]Department of Global Health Promotion, Tokyo Medical and Dental University, Tokyo, Japan
[23]Department of Medicinal Sciences, Graduate School of Pharmaceutical Sciences, Kyushu University, Fukuoka, Japan
[24]Global Station for Biosurfaces and Drug Discovery, Hokkaido University, Sapporo, Japan
[25]Division of Pathogen Structure, International Institute for Zoonosis Control, Hokkaido University, Sapporo, Japan
[26]HiLung Inc., Kyoto, Japan
[27]Tokyo Metropolitan Institute of Public Health, Tokyo, Japan
[28]One Health Research Center, Hokkaido University, Sapporo, Japan
[29]Graduate School of Biomedical and Health Sciences, Hiroshima University, Hiroshima, Japan
[30]Laboratory of Medical Virology, Institute for Life and Medical Sciences, Kyoto University, Kyoto, Japan
[31]AMED-CREST, Japan Agency for Medical Research and Development (AMED), Tokyo, Japan
[32]International Collaboration Unit, International Institute for Zoonosis Control, Hokkaido University, Sapporo, Japan
[33]Division of Risk Analysis and Management, International Institute for Zoonosis Control, Hokkaido University, Sapporo, Japan
[34]Laboratory of Virus Control, Research Institute for Microbial Diseases, Osaka University, Suita, Japan
[35]International Research Center for Infectious Diseases, The Institute of Medical Science, The University of Tokyo, Tokyo, Japan
[36]International Vaccine Design Center, The Institute of Medical Science, The University of Tokyo, Tokyo, Japan
[37]Graduate School of Frontier Sciences, The University of Tokyo, Kashiwa, Japan
[38]Collaboration Unit for Infection, Joint Research Center for Human Retrovirus infection, Kumamoto University, Kumamoto, Japan
[39]CREST, Japan Science and Technology Agency, Kawaguchi, Japan
[40]These authors contributed equally
[41]Twitter: @SystemsVirology
[42]Lead contact
*Correspondence: tanaka@med.hokudai.ac.jp (S.T.), ikedat@kumamoto-u.ac.jp (T.I.), fukut@pop.med.hokudai.ac.jp (T.F.), keisato@g.ecc.u-tokyo.ac.jp (K.S.)
https://doi.org/10.1016/j.chom.2022.10.003

Meng et al., 2022; Planas et al., 2021; Takashita et al., 2022; VanBlargan et al., 2022), BA.2 (Bruel et al., 2022; Takashita et al., 2022; Yamasoba et al., 2022b), and BA.5 (Yamasoba et al., 2022b; Khan et al., 2022; Wang et al., 2022; Qu et al., 2022; Hachmann et al., 2022; Tuekprakhon et al., 2022; Cao et al., 2022; Arora et al., 2022; Lyke et al., 2022; Gruell et al., 2022; Kimura et al., 2022c) exhibit profound resistance to neutralizing antibodies induced by vaccination, natural SARS-CoV-2 infection, and therapeutic monoclonal antibodies. In particular, newly spreading SARS-CoV-2 variants tend to be resistant to the humoral immunity induced by infection with a prior variant; for instance, BA.2 is resistant to BA.1 breakthrough infection sera (Qu et al., 2022; Tuekprakhon et al., 2022; Yamasoba et al., 2022a), and BA.5 is resistant to BA.2 breakthrough infection sera (Wang et al., 2022; Hachmann et al., 2022; Kimura et al., 2022c). Therefore, acquiring immune resistance to previously dominant variants is a key factor in outcompeting previous variants, thereby obtaining relatively increased R_e compared with the previously dominant variant. In addition to the evasion of humoral immunity induced by vaccination and infection, substitutions in the S protein can affect sensitivity to therapeutic monoclonal antibodies; for instance, BA.5 exhibits higher resistance to certain therapeutic antibodies than BA.2 (Yamasoba et al., 2022b; Wang et al., 2022; Cao et al., 2022). Furthermore, viral pathogenicity is closely associated with the phenotype of the viral S protein. In particular, we have proposed that the fusogenicity of the viral S protein in *in vitro* cell cultures is associated with viral pathogenicity *in vivo* (Kimura et al., 2022c; Yamasoba et al., 2022a; Suzuki et al., 2022; Saito et al., 2022).

As mentioned above, major SARS-CoV-2 phenotypes can be defined by the function of the viral S protein. The SARS-CoV-2 S protein has two major domains, the receptor-binding domain (RBD) and the N-terminal domain (NTD) (Mittal et al., 2022; Harvey et al., 2021). The RBD is crucial for the binding to the human angiotensin-converting enzyme 2 (ACE2) receptor for cell attachment and entry; therefore, this domain has been considered a major target for neutralizing antibodies to block viral infection (Harvey et al., 2021; Jackson et al., 2022; Barnes et al., 2020). The NTD can also be recognized by antibodies, and some antibodies targeting the NTD potentially neutralize viral infection (Lok, 2021; Voss et al., 2021; Cerutti et al., 2021; Suryadevara et al., 2021; McCallum et al., 2021; Liu et al., 2020; Chi et al., 2020), despite our limited understanding of its virological function.

The Omicron BA.2.75 variant, a new BA.2 subvariant, was first detected in India in May 2022 (WHO, 2022). Because an early preliminary investigation suggested the potential increase in the relative R_e value of BA.2.75 compared with that of BA.5 and the original BA.2 (GitHub, 2022), BA.2.75 has been flagged as the most concerning variant that can potentially outcompete BA.5 and become the next predominant variant in the future. On July 19, 2022, the WHO classified this variant as a variant of concern lineage under monitoring (WHO, 2022). Compared with the BA.2 S, BA.5 S has four mutations (Kimura et al., 2022c; Yamasoba et al., 2022a), whereas BA.2.75 S has nine mutations. These findings suggest that the virological phenotype of BA.2.75 is critically different from that of previous BA.2 subvariants. Here, we elucidate the features of a newly emerging SARS-CoV-2 Omicron BA.2.75 subvariant.

Please cite this article in press as: Saito et al., Virological characteristics of the SARS-CoV-2 Omicron BA.2.75 variant, Cell Host & Microbe (2022), https://doi.org/10.1016/j.chom.2022.10.003

CellPress
OPEN ACCESS

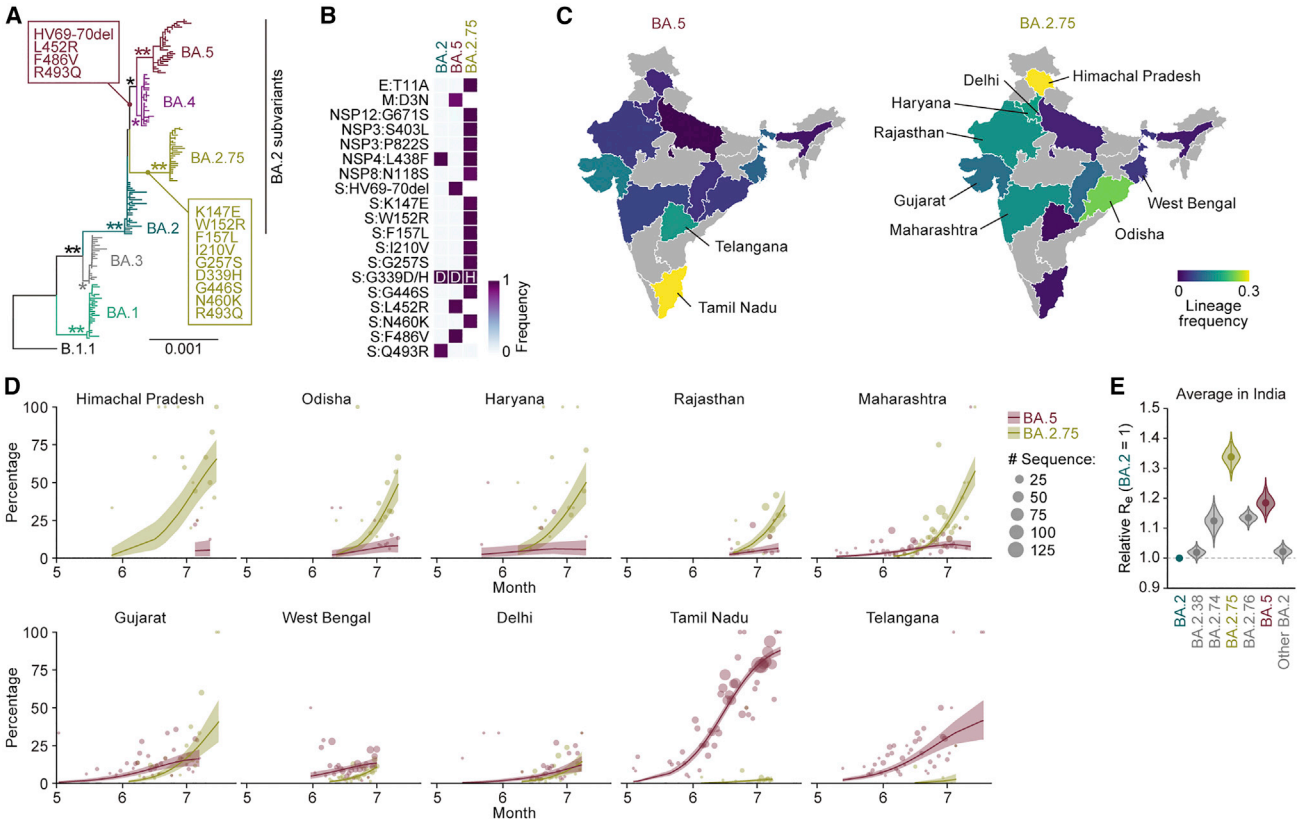

Figure 1. Epidemics of BA.2.75 in India

(A) A maximum likelihood tree of Omicron sublineages. Sequences of BA.1-BA.5 sampled from South Africa and BA.2.75 are included. The mutations acquired in the S protein of BA.2.75 are indicated. Note that R493Q is a reversion (i.e., back mutation from the BA.1–BA.3 lineages [R493] to the B.1.1 lineage [Q493]). Bootstrap values, *≥0.8; **≥0.95.

(B) Amino acid differences among BA.2, BA.2.75, and BA.5. Heatmap indicates the frequency of amino acid substitutions.

(C) Lineage frequencies of BA.5 (left) and BA.2.75 (right) in each Indian state. SARS-CoV-2 sequences collected from June 15 to July 15, 2022 were analyzed.

(D) Epidemic dynamics of SARS-CoV-2 lineages in Indian states. The results for BA.2.75 and BA.5 are shown. The observed daily sequence frequency (dot) and the dynamics (posterior mean, line; 95% CI, ribbon) are shown. The dot size is proportional to the number of sequences.

(E) Estimated relative R_e of each viral lineage, assuming a fixed generation time of 2.1 days. The R_e value of BA.2 is set at 1. The posterior (violin), posterior mean (dot), and 95% CI (line) are shown. The average values across India estimated by a Bayesian hierarchical model are shown, and the state-specific R_e values are shown in Figure S1B.

See also Figure S1 and Table S1.

RESULTS

Epidemics of BA.2.75 in India

As of the beginning of August 2022, the Omicron BA.5 variant is predominant worldwide. However, a novel BA.2 subvariant, BA.2.75, emerged and rapidly spread in India since May 2022. Although BA.2.75 and BA.5 belong to the BA.2 subvariant clade, BA.2.75 is phylogenetically distinct from the BA.5 clade (Figure 1A). Compared with BA.2, BA.2.75 harbors 14-amino-acid substitutions, including nine substitutions in the S protein (Figures 1B and S1A). In India, BA.5 and BA.2.75 spread in different regions: BA.5 spread in the southern area, including the Tamil Nadu and Telangana states, whereas BA.2.75 spread to the other areas, including the Himachal Pradesh, Odisha, Haryana, Rajasthan, and Maharashtra states (Figures 1C and 1D). To compare the relative R_e between BA.5 and BA.2.75 in India upon adjusting the regional differences, we constructed a Bayesian hierarchical model that can estimate both state-specific R_e values and the value averaged in India (Figures 1E and S1B; Table S1). The R_e value of BA.5 is 1.19-fold higher than that of BA.2 on average in India (Figure 1E). This value is comparable with the relative R_e value of BA.5 in South Africa (1.21) estimated in our recent study (Kimura et al., 2022c). Of note, the R_e value of BA.2.75 was 1.34-fold higher than that of BA.2, and the R_e value of BA.2.75 was 1.13-fold higher than that of BA.5 (Figures 1E and S1C). Furthermore, in the Indian states analyzed, the R_e value of BA.2.75 was greater than that of BA.5 (Figures S1B and S1C). Together, our data suggest that BA.2.75 has the potential to spread more rapidly than BA.5 and will be predominant in some regions including India in the near future.

Sensitivity of BA.2.75 to antiviral humoral immunity

To investigate the sensitivity of BA.2.75 to antiviral humoral immunity, we prepared pseudoviruses bearing the S proteins of D614G-bearing ancestral B.1.1, BA.2, BA.5, and BA.2.75.

Please cite this article in press as: Saito et al., Virological characteristics of the SARS-CoV-2 Omicron BA.2.75 variant, Cell Host & Microbe (2022), https://doi.org/10.1016/j.chom.2022.10.003

Human sera were collected from vaccinated and infected individuals (Table S2). The 2-dose vaccine sera were ineffective against all Omicron subvariants tested, including BA.2.75 (Figure 2A). Although BA.5 was significantly more resistant to 3-dose vaccine sera than BA.2, which is consistent with previous studies (Wang et al., 2022; Hachmann et al., 2022; Kimura et al., 2022c), the sensitivity of BA.2.75 to these sera was comparable with that of BA.2 (Figures 2B and 2C). However, BA.5 (2.1-fold) and BA.2.75 (1.7-fold) were significantly more resistant to 4-dose vaccine sera than BA.2 (Figure 2D). To identify the substitution(s) responsible for the higher resistance of BA.2.75 to 4-dose vaccine sera than BA.2, we prepared BA.2 S-based derivatives with the BA.2.75 substitutions. As shown in Figure 2D, four substitutions in the NTD, K147E, W152R, F157L, and I210V, and a substitution in the RBD, N460K, are responsible for the resistance to 4-dose vaccine sera. On the other hand, R493Q increased the sensitivity to 4-dose vaccine sera (Figure 2D). Since R493Q is a reversion substitution (R493 in BA.2 but Q493 in B.1.1, BA.5, and BA.2.75; Figure S1A), these results suggest that this substitution recovered the epitope recognized by vaccine-induced humoral immunity.

We then assessed the sensitivity of BA.2.75 to the convalescent sera from individuals who were infected with BA.1 or BA.2 after 2-dose or 3-dose vaccination (i.e., breakthrough infection). Similar to the previous reports including ours (Wang et al., 2022; Hachmann et al., 2022; Kimura et al., 2022c), BA.5 exhibited significant resistance to breakthrough infection sera compared with BA.2. In contrast, the sensitivity of BA.2.75 to these sera was comparable with that of BA.2 (Figures 2E and 2F), suggesting that BA.2.75 is not resistant to the humoral immunity induced by infection with prior Omicron subvariants, including BA.1 and BA.2. In the case of BA.5 breakthrough infection sera, both BA.2 (1.2-fold) and BA.2.75 (1.7-fold) were significantly more resistant than BA.5 (Figure 2G). The neutralization assay to screen the substitution(s) responsible for the higher resistance of BA.2.75 to breakthrough BA.5 infection sera showed that two substitutions in the NTD, K147E and W152R, and a substitution in the RBD, G446S, were responsible for the resistance to breakthrough BA.5 infection sera (Figure 2G).

To further address the difference in immunogenicity among Omicron subvariants, we used the sera obtained from infected hamsters at 16 days postinfection (d.p.i.) (Kimura et al., 2022c; Yamasoba et al., 2022a; Suzuki et al., 2022). Although the sera obtained from the BA.1-infected hamsters were ineffective against BA.2, BA.5, and BA.2.75 (Figure 2H), both BA.5 (9.7-fold) and BA.2.75 (13-fold) exhibited significantly greater resistance to the sera obtained from the BA.2-infected hamsters than BA.2 (Figure 2I). These results suggest that the immunogenicity of BA.5 and BA.2.75 is different from that of BA.2. Notably, BA.2 (7.1-fold) and BA.2.75 (11-fold) exhibited significant resistance to the sera obtained from BA.5-infected hamsters (Figure 2J). The assay using BA.2-based derivatives showed that G446S contributes to the resistance of BA.2.75 to the humoral immunity induced by BA.2 and BA.5 infections in hamsters (Figures 2I and 2J). Additionally, R493Q is associated with resistance to BA.2-induced hamster immunity (Figure 2I). Because the R493Q substitution is shared with BA.5 (Figures 1B and S1A), this substitution may contribute to the resistance of BA.5 to BA.2-induced immunity (Figure 2I). Finally, we used the sera obtained from hamsters infected with BA.2.75 at 16 d.p.i. for the neutralization assay. Compared with BA.2.75, BA.2 (3.4-fold) and BA.5 (6.4-fold) exhibited significant resistance to the sera obtained from the BA.2.75-infected hamsters (Figure 2K). Altogether, these results suggest that the immunogenicity of BA.2, BA.5, and BA.2.75 is different from each other.

Sensitivity of BA.2.75 to antiviral monoclonal antibodies and drugs

To analyze the sensitivity of BA.2.75 toward therapeutic monoclonal antibodies, we prepared ten monoclonal antibodies and three antibody cocktails. Adintrevimab, bamlanivimab, casirivimab, etesevimab, and imdevimab did not work against BA.2, BA.5, and BA.2.75 (Table 1; Figure S2A). Importantly, although regdanvimab, sotrovimab, and tixagevimab did not exhibit antiviral effects against BA.2 and BA.5, these three antibodies were functional against BA.2.75 (Table 1), suggesting that these antibodies can be used for the therapy and prevention of BA.2.75 infection. Consistent with our recent study (Yamasoba et al., 2022b), cilgavimab was less effective against BA.5 than BA.2, and BA.2.75 exhibited 24.4-fold higher resistance to cilgavimab than BA.2 (familywise error rate [FWER] = 0.04) (Table 1). Notably, although bebtelovimab exhibited robust antiviral effects against BA.2 and BA.5 (Yamasoba et al., 2022b), BA.2.75 was significantly more resistant to this antibody than BA.2 (21.2-fold, FWER = 0.01) and BA.5 (25.6-fold, FWER = 0.01) (Table 1).

Because BA.2.75 exhibited different sensitivities to five monoclonal antibodies, bebtelovimab, cilgavimab, regdanvimab, sotrovimab, and tixgevimab, from BA.2 (Table 1), we assessed the BA.2.75-specific substitution(s) that determine the sensitivity/resistance of BA.2.75. As shown in Figure S2B and Table S3, the resistance of BA.2.75 to bebtelovimab and cilgavimab is determined by the G446S substitution, which is present in the epitope of these two antibodies (Westendorf et al., 2022; Dong et al., 2021). The increased sensitivity of BA.2.75 to sotrovimab is attributed to the D339H substitution, whereas those to regdanvimab and tixagevimab are attributed to the R493Q reversion substitution (Figure S2B; Table S3). These observations are consistent with the fact that D339H and R493Q are present in the known epitopes of these antibodies (Dong et al., 2021; Pinto et al., 2020; Kim et al., 2021).

To evaluate the sensitivity of BA.2.75 to three antiviral drugs, remdesivir, EIDD-1931, and nirmatrelvir, we used clinical isolates of BA.2.75, B.1.1 (Suzuki et al., 2022), BA.2 (Kimura et al., 2022c), and BA.5 (Tamura et al., 2022). These viruses were inoculated into human airway organoids (AOs), a physiologically relevant model (Sano et al., 2022), and treated with three antiviral drugs. As shown in Figure S3 and Table 2, remdesivir had a stronger antiviral effect against BA.2.75 than against the other variants, B.1.1, BA.2, and BA.5. EIDD-1931 inhibited BA.2 and BA.2.75 more potently than B.1.1 and BA.5. For nirmatrelvir, no differences in antiviral efficacy were observed among the four variants. These results suggest that all three drugs exhibit antiviral effects against BA.2.75, and EIDD-1931 is particularly effective against BA.2.75.

Virological characteristics of BA.2.75 S *in vitro*

To investigate the virological properties of BA.2.75 S, we measured pseudovirus infectivity. As shown in Figure 3A, the

Please cite this article in press as: Saito et al., Virological characteristics of the SARS-CoV-2 Omicron BA.2.75 variant, Cell Host & Microbe (2022), https://doi.org/10.1016/j.chom.2022.10.003

CellPress
OPEN ACCESS

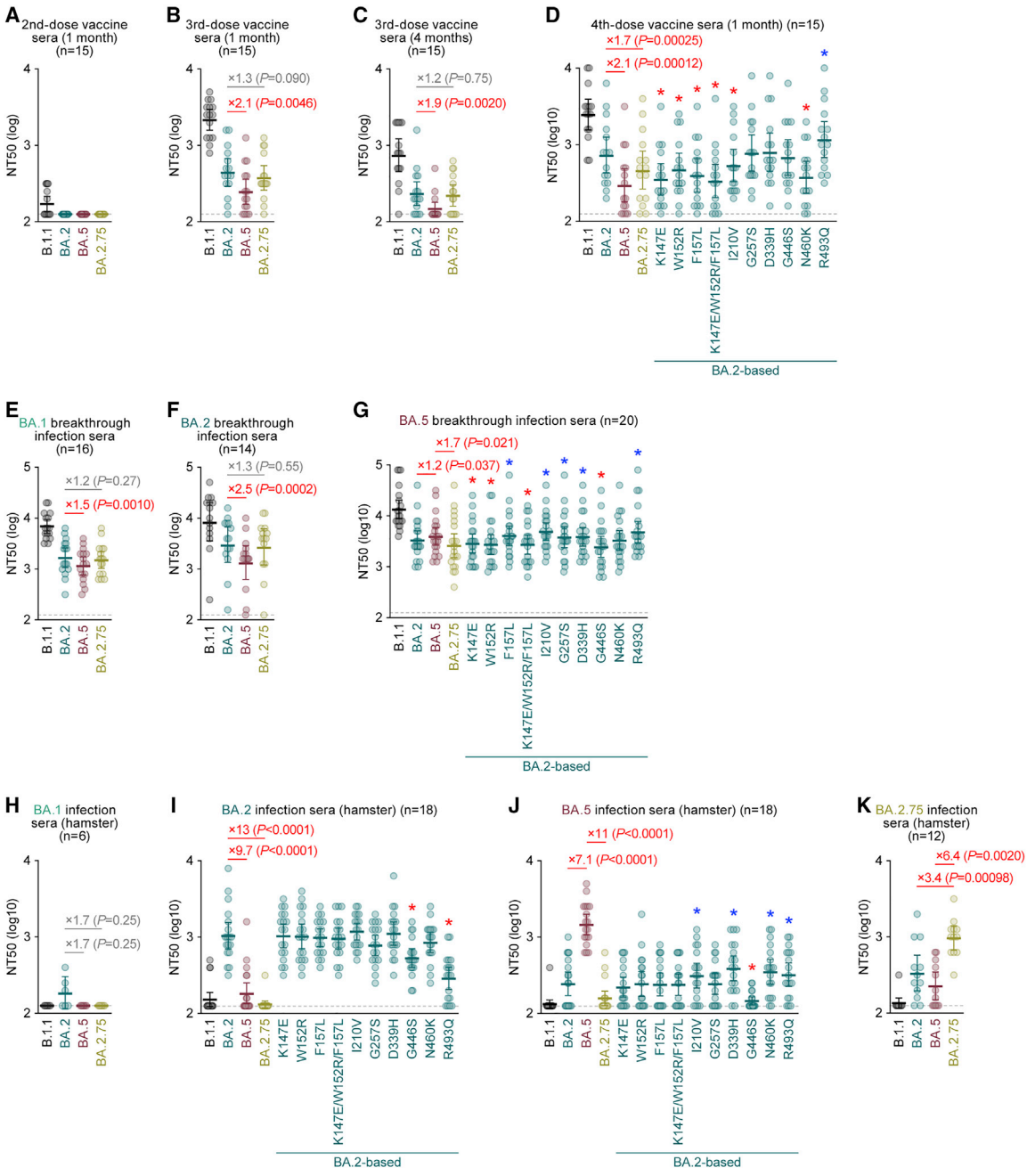

Figure 2. Immune resistance of BA.2.75

Neutralization assays were performed with pseudoviruses harboring the S proteins of B.1.1, BA.1, BA.2, and BA.2.75.

The BA.2 S-based derivatives are included in (D), (G), (I), and (J). The following sera were used.

(A–D) mRNA vaccine sera (15 donors) collected 1 month after the 2nd-dose vaccination (A), 1 month after the 3rd-dose vaccination (B), 4 months after the 3rd-dose vaccination (C), and 1 month after the 4th-dose vaccination (D).

(E–G) Convalescent sera from fully vaccinated individuals who had been infected with BA.1 after full vaccination (16 donors) (E), BA.2 after full vaccination (14 donors) (F), and BA.5 after full vaccination (20 donors) (G).

(H–K) Sera from hamsters infected with BA.1 (6 hamsters; H), BA.2 (18 hamsters; I), BA.5 (18 hamsters; J), and BA.2.75 (12 hamsters; K).

Assays for each serum sample were performed in triplicate to determine the 50% neutralization titer (NT_{50}). Each dot represents one NT_{50} value, and the geometric mean and 95% CI are shown. Statistically significant differences were determined by two-sided Wilcoxon signed-rank tests. The p values versus BA.2 (B–F, H, and I), BA.5 (G and J), or BA.2.75 (K) are indicated in the panels. The horizontal dashed line indicates the detection limit (120-fold). For the BA.2 derivatives (D, G, I, and J), statistically significant differences versus BA.2 ($p < 0.05$) are indicated with asterisks. Red and blue asterisks indicate decreased and increased NT_{50}s, respectively. Information on the vaccinated/convalescent donors is summarized in Table S2.

See also Table S2.

Please cite this article in press as: Saito et al., Virological characteristics of the SARS-CoV-2 Omicron BA.2.75 variant, Cell Host & Microbe (2022), https://doi.org/10.1016/j.chom.2022.10.003

Table 1. IC_{50} values of ten therapeutic monoclonal antibodies against BA.2.75

	B.1.1	BA.2	BA.4/5	BA.2.75
Adintrevimab	6.3 ± 1.7	>2,750	>2,750	>2,750
Bamlanivimab	6.7 ± 1.1	>4,725	>4,725	>4,725
Bebtelovimab	2.4 ± 0.9	1.7 ± 0.8	1.3 ± 0.3	34 ± 6.9 *†
Casirivimab	3.4 ± 1.2	>5,042	>5,042	2,303 ± 2,570
Cilgavimab	14 ± 1.7	21 ± 7.9	305 ± 127	479 ± 154 *
Etesevimab	12 ± 1.6	>4,600	>4,600	>4,600
Imdevimab	8.0 ± 3.1	>5,000	>5,000	>5,000
Regdanvimab	1.0 ± 0.4	>4,025	>4,025	42 ± 14 *†
Sotrovimab	47 ± 50	1,213 ± 224	1,149 ± 159	240 ± 56 *†
Tixagevimab	1.5 ± 0.6	3,815 ± 1,032	>4,375	45 ± 8.2 *†
Ronapreve (casirivimab + imdevimab)	3.9 ± 2.3	>5,000	>5,000	>5,000
Evusheld (cilgavimab + tixagevimab)	4.7 ± 1.1	42 ± 17	586 ± 193	113 ± 31 *
Etesevimab + bamlanivimab	8.3 ± 1.0	>4,600	>4,600	>4,600

The average 50% inhibitory concentration (IC_{50}; ng/mL) ± 95% confidence interval is shown. Statistical significance was evaluated by the Welch t test with multiple testing corrections by the Holm method. An asterisk (*) and dagger (†) denote FWER < 0.05 for the BA.2.75 versus BA.2 and BA.2.75 versus BA.4/5 comparisons, respectively. Representative neutralization curves are shown in Figure S2.

pseudovirus infectivity of BA.2.75 was significantly (12.5-fold) higher than that of BA.2. To assess the association of TMPRSS2 usage with the increased pseudovirus infectivity of BA.2.75, we used both HEK293-ACE2/TMPRSS2 cells and HEK293-ACE2 cells, on which endogenous surface TMPRSS2 is undetectable (Yamasoba et al., 2022a), as target cells. As shown in Figure S4A, the infectivity of BA.2.75 pseudovirus was not increased by TMPRSS2 expression (Figure S4A), suggesting that TMPRSS2 is not associated with an increase in pseudovirus infectivity of BA.2.75. To determine the substitutions that are responsible for the increased pseudovirus infectivity of BA.2.75, we used a series of BA.2 derivatives that bear the BA.2.75-specific substitutions. Three substitutions in the NTD, K147E, F157L, and I210V, and two substitutions in the RBD, N460K and R493Q, significantly increased infectivity (Figure 3A). Notably, the N460K substitution increased infectivity by 44-fold (Figure 3A). However, a substitution in the NTD, W152R, significantly (8.9-fold) decreased infectivity (Figure 3A). The BA.2 derivative bearing the three substitutions in the NTD in close proximity to each other, K147E, W152R, and F157L, exhibited comparable infectivity with BA.2 (Figure 3A).

We next measured the ACE2 binding affinity of the RBDs of BA.2.75 as well as those of BA.2 derivatives bearing D339H, G446S, N460K, and R493Q substitutions by an enhanced yeast surface display system (Zahradník et al., 2021a). Intriguingly, the BA.2.75 RBD showed a strong tight binding with an affinity of 146 ± 6 pM (Figure 3B). Consistent with the results of the pseudovirus assay (Figure 3A), the BA.2 N460K substitution exhibited a significantly increased binding affinity compared with BA.2 (Figure 3B). To assess the impact of N460K in BA.2.75 S, we prepared the BA.2.75 RBD derivative bearing the K460N reversion substitution. As shown in Figure 3B, the BA.2.75 K460N substitution exhibited a significantly reduced binding affinity compared with BA.2.75. These observations suggest that N460K is a critical substitution in the BA.2.75 S to increase viral infectivity by enhancing binding affinity to ACE2.

To reveal the structural effect of the N460K substitution, we performed cryoelectron microscopy (cryo-EM) analysis of the BA.2.75 S ectodomain and the complex of the BA.2.75 S ectodomain and human ACE2, which determined cryo-EM maps with C1 symmetry at resolutions of 2.86 Å (closed 1) and 3.48 Å, respectively (Figure 3C; Table S4). The ectodomain of BA.2.75 S showed three different conformational states (mol ratio, 4.5:2.5:3.0), with two closed states with all RBDs "down," but these maps were reconstructed with slightly different RBD conformations, and an open state with one RBD "up" and two RBD "down" (Figures S4B and S4C; Table S4). There are four-amino-acid substitutions in the RBD of BA.2.75 S compared with BA.2. G446S and R493Q are located on the receptor-binding motif (RBM), whereas N460K and D339H are located distal to the RBM (Figure 3D, left). N460K forms an intramolecular salt bridge with D420, suggesting that N460K may contribute to RBD folding/flexibility (Figure 3D, upper right). However, at a low resolution, the electron density map of the BA.2.75 S and ACE2 complex showed the same binding mode as that of ACE2 bound to the RBDs of other SARS-CoV-2 variants (Figures 3C right, S4B, and S4C; Table S4). Therefore, this binding mode suggested that N460K is in a position close to the *N*-linked glycan on the N90 residue of ACE2 (Figure 3E). Interestingly, a previous study showed that the glycan linked to the N90 residue of ACE2 exhibits an inhibitory effect on binding to the S proteins of previous SARS-CoV-2 variants (Chan et al., 2020). To test the possible association of the *N*-linked glycan on the N90 residue of ACE2 with the increased binding affinity of BA.2.75 S to ACE2, we performed an additional round of binding experiments using the human ACE2 receptor bearing the N90Q substitution, which ablates the *N*-linked glycosylation. Consistent with the previous study (Chan et al., 2020), the ACE2 N90Q substitution increased the binding affinity of BA.2 S RBD (Figure 3F). On the other hand, the binding affinity of BA.2.75 RBD was significantly reduced by the N90Q substitution of ACE2 (Figure 3F). Altogether, our findings suggest the increased binding affinity of BA.2.75 S is partly attributed to the interaction of BA.2.75 S K460 residue to the *N*-linked glycan on the N90 residue of ACE2.

In addition to N460K, the structure of the BA.2.75 S ectodomain showed that D339H forms an intramolecular interaction with F371 (Figure 3D, bottom right). This observation suggests that D339H possibly contributes to the improved folding/flexibility of RBD. In particular, D339H requires two nucleotide changes in the codon to occur. Such changes are still relatively rare in the evolution of SARS-CoV-2, reinforcing the importance and corresponding fitness advantage. To analyze the potential impact of this substitution, we additionally prepared the BA.2.75 RBD derivative bearing H339D and measured its affinity. As shown in Figure 3B, the K_D value of this derivative was

Please cite this article in press as: Saito et al., Virological characteristics of the SARS-CoV-2 Omicron BA.2.75 variant, Cell Host & Microbe (2022), https://doi.org/10.1016/j.chom.2022.10.003

Table 2. Effects of three antiviral drugs against BA.2.75 in AOs

	EC_{50} (μM)				EC_{50} ratio				
	B.1.1	BA.2	BA.5	BA.2.75	BA.5/BA.2	BA.2.75/BA.2	BA.2/B.1.1	BA.5/B.1.1	BA.2.75/B.1.1
Remdesivir	1.08	1.89	1.31	0.63	0.70	0.34	1.75	1.21	0.59
EIDD-1931	0.24	0.02	0.21	0.08	8.82	3.53	0.10	0.89	0.36
Nirmatrelvir	0.84	0.85	0.63	0.81	0.74	0.95	1.02	0.75	0.97

Representative inhibition curves are shown in Figure S3.

significantly (3-fold) higher than that of the parental BA.2.75, suggesting that D339H appears to indirectly affect the affinity for ACE2.

To further reveal the virological property of BA.2.75 S, we performed a cell-based fusion assay (Kimura et al., 2022b, 2022c; Yamasoba et al., 2022a; Suzuki et al., 2022; Saito et al., 2022; Motozono et al., 2021) using Calu-3 cells as target cells. Flow cytometry analysis showed that the surface expression level of BA.2.75 was comparable with that of BA.2 (Figure 3G). Consistent with our recent study (Kimura et al., 2022c), the fusogenicity of BA.5 was significantly higher than that of BA.2, and notably, BA.2.75 S was also significantly more fusogenic than BA.2 S (Figure 3H). Moreover, a coculture experiment using HEK293-ACE2/TMPRSS2 cells as the target cells (Kimura et al., 2022c; Yamasoba et al., 2022a; Suzuki et al., 2022) showed that the S proteins of BA.5 and BA.2.75 showed significantly increased fusogenicity compared with that of BA.2 S (Figure S4D). Altogether, these results suggest that BA.2.75 S exhibits higher binding affinity to human ACE2 and higher fusogenicity.

Virological characteristics of the BA.2.75 clinical isolate *in vitro*

To evaluate the growth capacity of BA.2.75, we inoculated clinical isolates of BA.2.75, B.1.1 (Suzuki et al., 2022), Delta (Saito et al., 2022), BA.2 (Kimura et al., 2022c), and BA.5 (Tamura et al., 2022) in a variety of *in vitro* cell culture systems. The growth efficacy of B.1.1 and Delta was significantly higher than that of BA.2 in Vero cells (Figure 4A), VeroE6/TMPRSS2 cells (Figure 4B), HEK293-ACE2/TMPRSS2 cells (Figure 4C), the AO-derived air-liquid interface (AO-ALI) model (Figure 4D), human induced pluripotent stem cell (iPSC)-derived airway epithelial cells (Figure 4E), and lung epithelial cells (Figure 4F). BA.5 replicated more efficiently than BA.2 with statistically significant differences in all cell culture systems except AO-ALI (Figures 4A–4F). The growth efficacy of BA.2.75 was significantly higher than that of BA.2 in Vero cells (Figure 4A), VeroE6/TMPRSS2 cells (Figure 4B), HEK293-ACE2/TMPRSS2 cells (Figure 4C), and iPSC-derived lung epithelial cells (Figure 4F), whereas the growth efficacy of BA.2.75 and BA.2 was comparable in the two airway epithelial cell systems (Figures 4D and 4E).

To evaluate the effect of BA.2.75 on the airway epithelial and endothelial barriers, we used airway-on-a-chips system (Figure S4E; Hashimoto et al., 2022). By measuring the amount of virus that invades from the top channel (Figure 4G) to the bottom channel (Figure 4H), we could evaluate the ability of viruses to disrupt the airway epithelial and endothelial barriers. Notably, the amount of virus that invaded the blood vessel channel of BA.2.75-, BA.5-, and B.1.1-infected airway-on-chips was significantly higher than that of BA.2-infected airway-on-chips (Figure 4I). These results suggest that BA.2.75 exhibits more severe airway epithelial and endothelial barrier disruption than BA.2.

To further address the fusogenic capacity of BA.2.75, we performed a plaque assay using VeroE6/TMPRSS2 cells. Consistent with our previous studies with a Delta isolate (Saito et al., 2022) as well as the recombinant SARS-CoV-2 bearing the B.1.1 S (Yamasoba et al., 2022a), BA.2 S (Yamasoba et al., 2022a), and BA.5 S (Kimura et al., 2022c), the plaques formed by the infections of clinical isolates of B.1.1, Delta, and BA.5 were significantly larger than those formed by the infection of BA.2 (Figure 4J). Notably, BA.2.75 infection also resulted in significantly larger plaques than BA.2 infection (Figure 4J). Together with the results of the cell-based fusion assay (Figure 3H) and airway-on-a-chip infection experiments (Figures 4G–4I), these observations suggest that BA.2.75 is more fusogenic than BA.2, and the fusogenicity of BA.2.75 is comparable with that of BA.5.

Virological characteristics of BA.2.75 *in vivo*

As we proposed in our prior studies (Kimura et al., 2022c; Yamasoba et al., 2022a; Suzuki et al., 2022; Saito et al., 2022), the fusogenicity of the S proteins of SARS-CoV-2 variants is closely associated with the intrinsic pathogenicity in an experimental hamster model. Given that BA.2.75 is more fusogenic than BA.2 in the *in vitro* cell culture systems (Figures 3 and 4), it is hypothesized that BA.2.75 is intrinsically more pathogenic than BA.2. To address this possibility, we intranasally inoculated a BA.2.75 isolate into hamsters. As controls, we also used clinical isolates of Delta, BA.2, and BA.5. Although we followed our established experimental protocol (Kimura et al., 2022c; Yamasoba et al., 2022a; Suzuki et al., 2022; Saito et al., 2022), the viral titers of clinical isolates of Omicron subvariants were relatively low. Therefore, we set out to conduct animal experiments in this study with relatively lower inocula (1,000 50% tissue culture infectious dose [$TCID_{50}$] [Figure 5A, top] or 5,000 $TCID_{50}$ [Figure 5A, bottom] per hamster) than our previous studies (10,000 $TCID_{50}$ per hamster) (Kimura et al., 2022c; Yamasoba et al., 2022a; Suzuki et al., 2022; Saito et al., 2022). Nevertheless, consistent with our previous study (Saito et al., 2022), Delta infection resulted in weight loss in the infection group with a higher inoculum (Figure 5A, bottom). At both challenge doses, the body weights of the BA.5- and BA.2.75-infected hamsters were significantly lower than those of the BA.2-infected hamsters (Figure 5A).

We then analyzed the pulmonary function of infected hamsters as reflected by three parameters, enhanced pause (Penh), the ratio of time to peak expiratory flow relative to the total expiratory time (Rpef), and breath per minute (BPM), which are surrogate markers for bronchoconstriction or airway obstruction.

Please cite this article in press as: Saito et al., Virological characteristics of the SARS-CoV-2 Omicron BA.2.75 variant, Cell Host & Microbe (2022), https://doi.org/10.1016/j.chom.2022.10.003

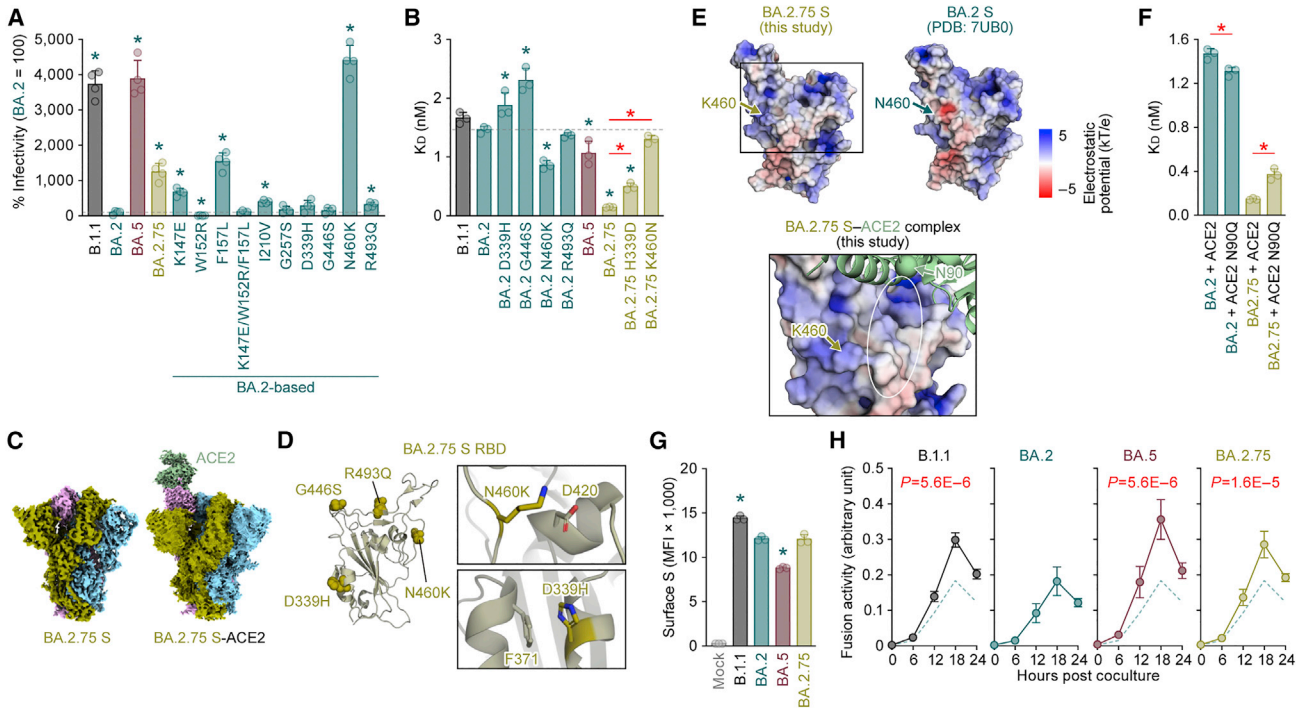

Figure 3. Virological features of BA.2.75 S *in vitro*

(A) Pseudovirus assay. The percent infectivity compared with that of the virus pseudotyped with the BA.2 S protein are shown.

(B) Binding affinity of the RBD of SARS-CoV-2 S protein to ACE2 by yeast surface display. The K_D value indicating the binding affinity of the RBD of the SARS-CoV-2 S protein to soluble ACE2 when expressed on yeast is shown.

(C) Overall cryo-EM map of SARS-CoV-2 BA.2.75 S (closed state 1, left) and BA.2.75 S (open state) bound to ACE2 receptor (right).

(D) Left, position of the four substitutions, D339H, G446S, N460K, and R493Q, in BA.2.75 S RBD. Right, close-up views of the interaction details of the two independent interfaces of BA.2.75 S.

(E) (Top) Electrostatic potential of BA.2.75 RBD (left) and BA.2 RBD (PDB: 7UB0, right) (Lan et al., 2020). The area indicated in square is shown in the bottom panel. (Bottom) BA.2.75 S RBD-human ACE2 complex. BA.2.75 S RBD is shown in surface. Human ACE2 is shown in green cartoon, and a putative N90-glycan of ACE2 is indicated in a circle. Electrostatic potential surface depictions calculated by APBS electrostatic plug-in (Jurrus et al., 2018) of PyMOL. The scale bar shows the electrostatic charge (kT/e).

(F) Binding affinity of the RBD of SARS-CoV-2 S protein to the ACE2 bearing the N90Q substitution by yeast surface display.

(G and H) S-based fusion assay. (G) S protein expression on the cell surface. The summarized data are shown. (H) S-based fusion assay in Calu-3 cells. The recorded fusion activity (arbitrary units) is shown. The dashed green line indicates the results of BA.2.

Assays were performed in quadruplicate (A and H) or triplicate (B, F, and G), and the presented data are expressed as the average ± SD. In (A) and (B), the dashed horizontal lines indicate the value of BA.2. In (A), (B), (F), and (G), each dot indicates the result of an individual replicate. In (A), (B), and (G), statistically significant differences between BA.2 and other variants (*$p < 0.05$) were determined by two-sided Student's t tests. In (B) and (F), red asterisks indicate statistically significant differences ($p < 0.05$) determined by two-sided Student's t tests. In (H), statistically significant differences between BA.2 and other variants across time points were determined by multiple regression. FWERs calculated using the Holm method are indicated in the figures.

See also Figure S4 and Table S4.

Subcutaneous oxygen saturation (SpO_2) was routinely measured in the group with the lower inoculum (Figure 5A, top). Although the SpO_2 values were comparable among the five groups, Delta infection resulted in significant differences in the other three respiratory parameters compared with BA.2 (Figure 5A), suggesting that Delta is more pathogenic than BA.2. In the group with a lower inoculum, although the values of Penh and Rpef of the hamsters infected with BA.2, BA.5, and BA.2.75 were comparable, the BPM value of BA.2.75 was significantly lower than that of BA.2 (Figure 5A, top). In the group with a higher inoculum, although the values of Penh and Rpef of the BA.5-infected hamsters were comparable with those of the BA.2-infected hamsters, these two values indicated that BA.2.75 infection leads to more severe disorder compared with BA.2 infection with statistical significance (Figure 5A, bottom). These results suggest that BA.2.75 is more pathogenic than BA.2.

To address the viral spread in infected hamsters, we routinely measured the viral RNA load in the oral swab. Although the viral RNA loads of the hamsters infected with Delta, BA.2, and BA.5 were comparable, the viral load in the swabs of the BA.2.75-infected hamsters was relatively highly maintained by 7 d.p.i. and was significantly higher than that of the BA.2-infected hamsters (Figure 5B). To address the possibility that BA.2.75 more efficiently spread in the respiratory tissues, we collected the lungs of infected hamsters at 2 and 5 d.p.i., and the collected tissues were separated into the hilum and periphery regions. Although the viral RNA loads in both the hilum and periphery of the four infection groups were comparable at 2 d.p.i. (Figure 5C, top), those of the hamsters infected with Delta, BA.5, and

Please cite this article in press as: Saito et al., Virological characteristics of the SARS-CoV-2 Omicron BA.2.75 variant, Cell Host & Microbe (2022), https://doi.org/10.1016/j.chom.2022.10.003

CellPress
OPEN ACCESS

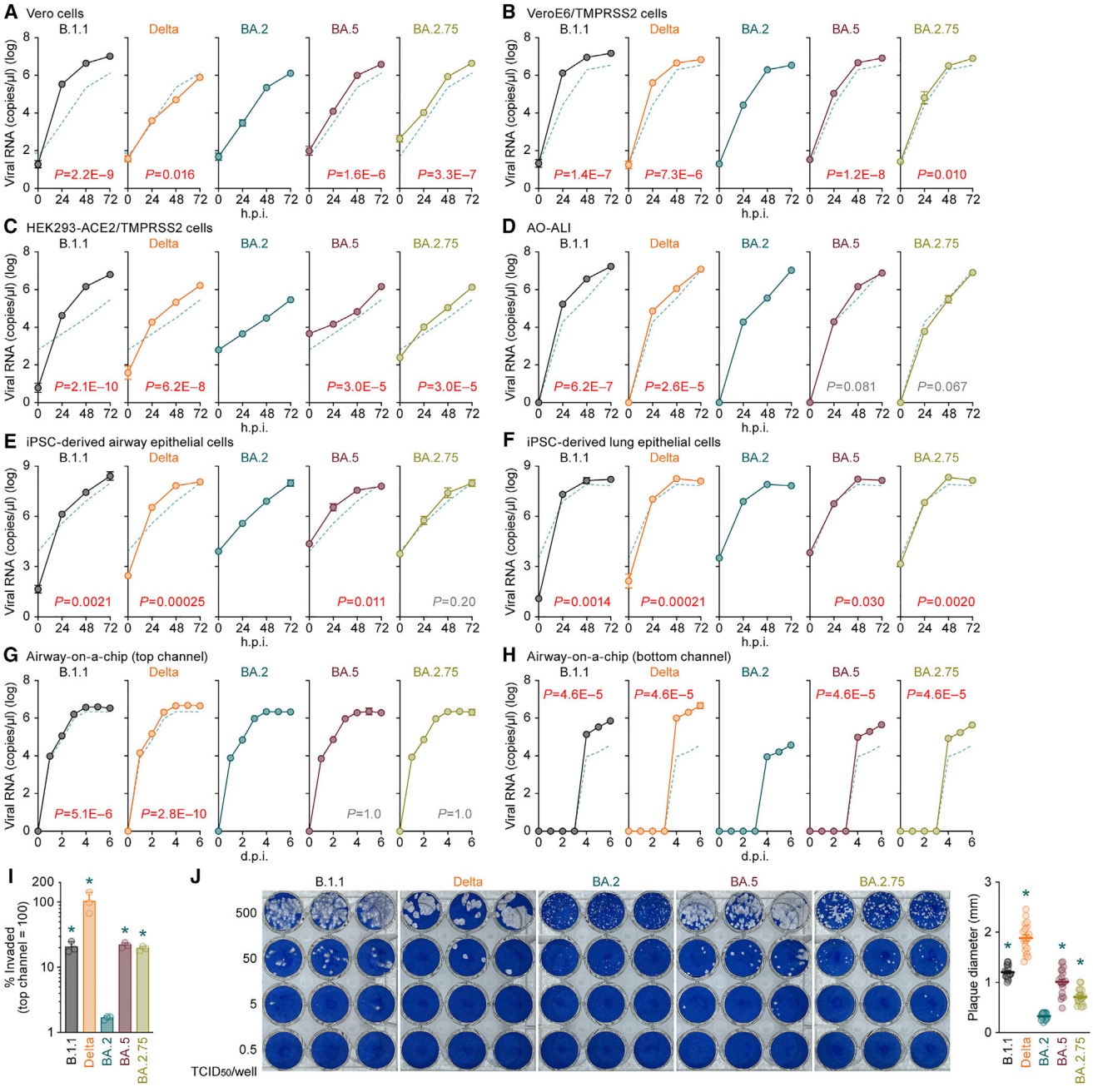

Figure 4. Growth capacity of BA.2.75 *in vitro*

(A–I) Growth kinetics of B.1.1, Delta, BA.2, BA.5, and BA.2.75. Clinical isolates of B.1.1, Delta, BA.2, BA.5, and BA.2.75 were inoculated into Vero cells (A), VeroE6/TMPRSS2 cells (B), HEK293-ACE2/TMPRSS2 cells (C), AO-ALI (D), iPSC-derived airway epithelial cells (E), iPSC-derived lung epithelial cells (F), and an airway-on-a-chip system (G and H; see also Figure S3C). The copy numbers of viral RNA in the culture supernatant (A–C), the apical sides of cultures (D–F), and the top (G) and bottom (H) channels of an airway-on-a-chip were routinely quantified by RT-qPCR. The dashed green line in each panel indicates the results of BA.2. In (I), the percentage of viral RNA load in the bottom channel per top channel at 6 d.p.i. (i.e., % invaded virus from the top channel to the bottom channel) is shown. (J) Plaque assay. Representative panels (left) and a summary of the recorded plaque diameters (20 plaques per virus) (right) are shown.

Assays were performed in quadruplicate, and the presented data are expressed as the average ± SD. In (A)–(H), statistically significant differences between BA.2 and the other variants across time points were determined by multiple regression. FWERs calculated using the Holm method are indicated in the figures. In (I) and (J) (right), statistically significant differences versus BA.2 (*$p < 0.05$) were determined by two-sided Mann-Whitney U tests. Each dot indicates the result of an individual replicate.

See also Figure S4.

Please cite this article in press as: Saito et al., Virological characteristics of the SARS-CoV-2 Omicron BA.2.75 variant, Cell Host & Microbe (2022), https://doi.org/10.1016/j.chom.2022.10.003

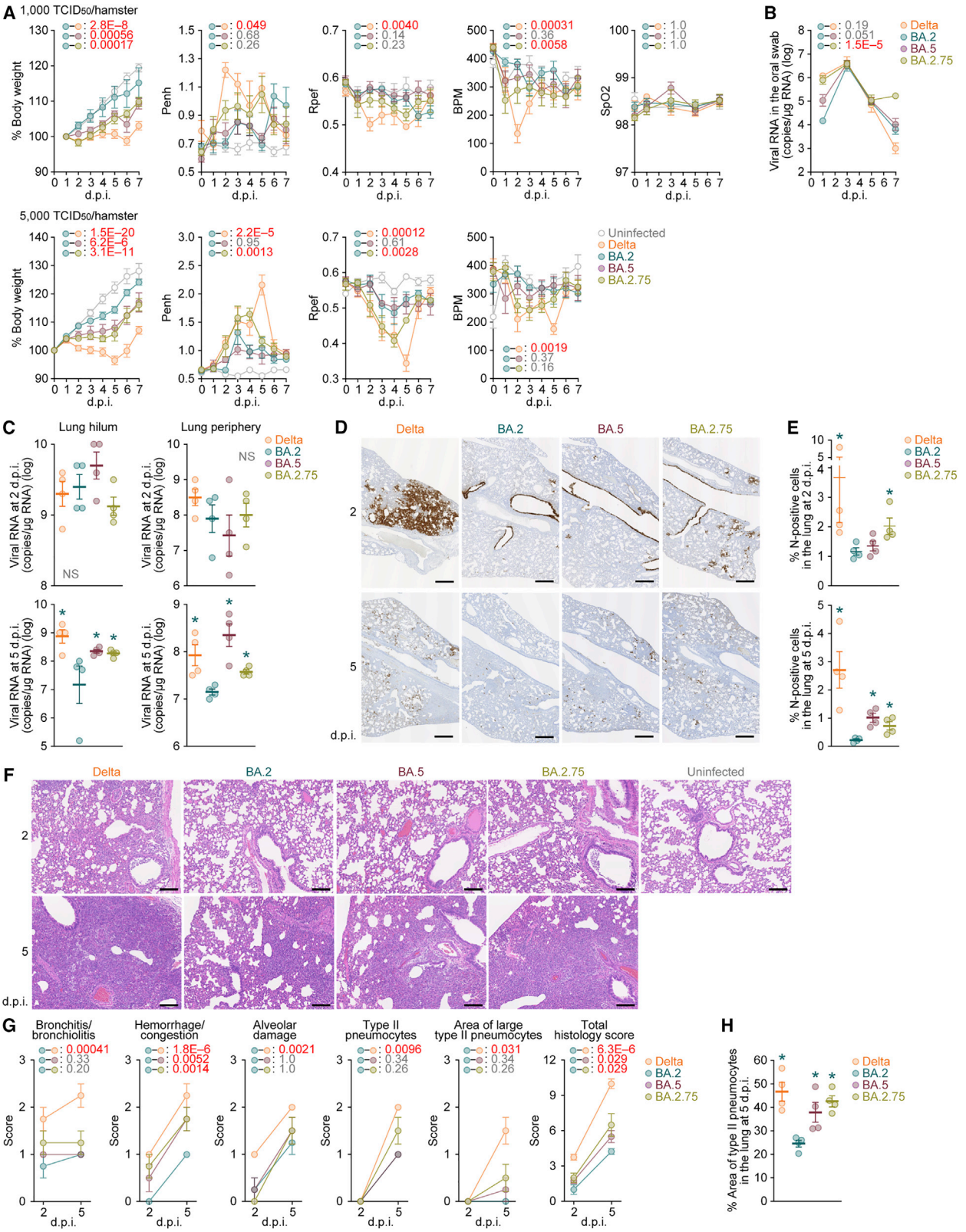

Figure 5. Virological characteristics of BA.2.75 *in vivo*

Syrian hamsters were intranasally inoculated with Delta, BA.2, BA.5, and BA.2.75. Two different doses of inoculum (1,000 $TCID_{50}$/hamster [A, top and B–G] or 5,000 $TCID_{50}$/hamster [A, bottom]) were used. Six hamsters per infection group were used to routinely measure the respective parameters (A and B). Four

(legend continued on next page)

Please cite this article in press as: Saito et al., Virological characteristics of the SARS-CoV-2 Omicron BA.2.75 variant, Cell Host & Microbe (2022), https://doi.org/10.1016/j.chom.2022.10.003

BA.2.75 were significantly higher than those infected with BA.2 at 5 d.p.i. (Figure 5C, bottom).

To further address virus spread in the respiratory tissues, we performed immunohistochemical (IHC) analysis targeting viral nucleocapsid (N) protein. Similar to our previous studies (Kimura et al., 2022c; Yamasoba et al., 2022a; Suzuki et al., 2022), epithelial cells in the upper tracheae of infected hamsters were sporadically positive for viral N protein at 2 d.p.i., but there were no significant differences among the four viruses, including BA.2.75 (Figure S5A). In the alveolar space around the bronchi/bronchioles at 2 d.p.i., N-positive cells were detected in Delta-infected hamsters. However, the N proteins strongly remained in the lobar bronchi in BA.5- and BA.2.75-infected hamsters (Figures 5D, top and S5B). Although few N-positive cells were detected in the alveolar space of the BA.2- and BA.5-infected hamsters, the N positivity spread into the alveolar space in the BA.2.75-infected hamsters (Figures 5D, top and S5B). The quantification of the N-positive area in four lung lobes at 2 d.p.i. (Figure S5B) showed that the N-positive areas of the Delta- and BA.2.75-infected hamsters were significantly greater than those of the BA.2-infected hamsters (Figure 5E, top). At 5 d.p.i., although the N-positive cells were barely detected in the lungs infected with BA.2, a few N-positive cells were detected in the peripheral alveolar space in the Delta, BA.5, and BA.2.75 groups (Figures 5D, bottom and S5C). The quantification of the N-positive area in the four lung lobes at 5 d.p.i. (Figure S5C) further showed that the N-positive areas of the Delta-, BA.5-, and BA.2.75-infected hamsters were significantly greater than those of the BA.2-infected hamsters (Figure 5E, bottom). These data suggest that BA.2 infects a smaller portion of the bronchial/bronchiolar epithelium because it is less efficiently transmitted to neighboring epithelial cells. In contrast, BA.5 and BA.2.75 infections seemed to persist in the bronchial/bronchiolar epithelium, and in particular, BA.2.75 invaded the alveolar space more efficiently than BA.5 at the early stage of infection. Altogether, the IHC data suggest that among Omicron subvariants, BA.2.75 more efficiently spread into the alveolar space than BA.2 and BA.5, with persistent infection in the bronchi/bronchioles.

Pathogenicity of BA.2.75

To investigate the intrinsic pathogenicity of BA.2.75, we analyzed the formalin-fixed right lungs of infected hamsters at 2 and 5 d.p.i. by carefully identifying the four lobules and main bronchus and lobar bronchi sectioning each lobe along with the bronchial branches. Histopathological scoring was performed according to the criteria described in our previous studies (Kimura et al., 2022c; Yamasoba et al., 2022a; Suzuki et al., 2022; Saito et al., 2022). Consistent with our previous studies (Suzuki et al., 2022; Saito et al., 2022), all five parameters as well as the total score of the Delta-infected hamsters were significantly higher than those of the BA.2-infected hamsters (Figures 5F and 5G). When we compared the histopathological scores of Omicron subvariants, the scores indicating hemorrhage or congestion and total histology scores of BA.5 and BA.2.75 were significantly greater than those of BA.2 (Figures 5F and 5G). Similar to our recent studies (Kimura et al., 2022c; Tamura et al., 2022), BA.5 is intrinsically more pathogenic than BA.2, and notably, our results suggest that BA.2.75 exhibits more significant inflammation than BA.2. For determination of the area of pneumonia, the inflammatory area was termed the area of type II pneumocytes and was morphometrically analyzed (Figure S5D). As summarized in Figure 5H, at 5 d.p.i., the percentages of the area of type II pneumocytes of Delta, BA.5, and BA.2.75 were significantly higher than that of BA.2. Altogether, these findings suggest that BA.2.75 infection intrinsically induces greater inflammation and exhibits higher pathogenicity than BA.2.

DISCUSSION

Here, we characterized the properties of the Omicron BA.2.75 variant, such as the growth rate in the human population, resistance to antiviral humoral immunity and antiviral drugs, functions of the S protein *in vitro*, and intrinsic pathogenicity. In terms of the emergence geography and phylogeny, BA.5 and BA.2.75 emerged independently. Nevertheless, the results of the cell-based fusion assay, airway-on-a-chip assay, and plaque assay suggested that both BA.5 and BA.2.75 acquired higher

hamsters per infection group at a lower inoculum (1,000 $TCID_{50}$/hamster) were euthanized at 2 and 5 d.p.i. and used for virological and pathological analysis (C–G).

(A) Body weight, Penh, Rpef, BPM, and SpO_2 values of infected hamsters (n = 6 each). The results at a low inoculum (1,000 $TCID_{50}$/hamster) and a high inoculum (5,000 $TCID_{50}$/hamster) are shown in the top and bottom panels, respectively.

(B) Viral RNA loads in the oral swab (n = 6 each).

(C) Viral RNA loads in the lung hilum (left) and lung periphery (right) of infected hamsters (n = 4 each) at 2 d.p.i. (top) and 5 d.p.i. (bottom).

(D and E) IHC of the viral N protein in the lungs at 2 d.p.i. (top) and 5 d.p.i. (bottom) of all infected hamsters. (D) Representative figures. N-positive cells are shown in brown. (E) Percentage of N-positive cells in whole lung lobes (n = 4 each). The raw data are shown in Figures S5B and S5C.

(F and G) (F) H&E staining of the lungs of infected hamsters. Representative figures are shown. Uninfected lung alveolar space and bronchioles are also shown. (G) Histopathological scoring of lung lesions (n = 4 each). Representative pathological features are reported in our previous studies (Kimura et al., 2022c; Yamasoba et al., 2022a; Suzuki et al., 2022; Saito et al., 2022).

(H) Type II pneumocytes in the lungs of infected hamsters. The percentage of the area of type II pneumocytes in the lung at 5 d.p.i. is summarized. The raw data are shown in Figure S5D.

In (A)–(C), (E), (G), and (H), data are presented as the average ± SEM. In (C), (E), and (H), each dot indicates the result of an individual hamster.

In (A), (B), and (G), statistically significant differences between BA.2 and other variants across time points were determined by multiple regression. In (A), the 0 d.p.i. data were excluded from the analyses. FWERs calculated using the Holm method are indicated in the figures.

In (C), (E), and (G), the statistically significant differences between BA.2 and other variants were determined by a two-sided Mann-Whitney U test.

In (D) and (F), each panel shows a representative result from an individual infected hamster. Scale bars: 500 μm in (D) and 200 μm in (F).

See also Figure S5.

Please cite this article in press as: Saito et al., Virological characteristics of the SARS-CoV-2 Omicron BA.2.75 variant, Cell Host & Microbe (2022), https://doi.org/10.1016/j.chom.2022.10.003

fusogenicity after divergence from BA.2. Our data, including a recent study (Kimura et al., 2022c), suggest that the critical substitution responsible for the higher fusogenicity of the BA.5 and BA.2.75 S proteins are different: the L452R substitution for BA.5 S and the D339H/N460K substitutions for BA.2.75 S.

In our previous studies focusing on Delta (Saito et al., 2022), Omicron BA.1 (Suzuki et al., 2022), BA.2 (Yamasoba et al., 2022a), and BA.5 (Kimura et al., 2022c), we proposed a close association between S-mediated fusogenicity *in vitro* and pathogenicity in a hamster model. Consistent with our hypothesis, we demonstrated that compared with BA.2, BA.2.75 exhibits higher fusogenicity *in vitro* and efficient viral spread in the lungs of infected hamsters, which leads to enhanced inflammation in the lung and higher pathogenicity *in vivo*. However, viral load is not necessarily associated with pathogenicity. Moreover, *in vitro* experiments using a variety of cell culture systems showed that BA.2.75 replicates more efficiently than BA.2 in alveolar epithelial cells but not in airway epithelial cells. Altogether, our results suggest that BA.2.75 exhibits higher fusogenicity and pathogenicity via evolution of its S protein independent of BA.5.

Using hamster sera, we demonstrated that the immunogenicity of BA.5 and BA.2.75 is different from each other, whereas BA.2.75 and BA.5 are the descendants of BA.2. However, the antiviral effect of BA.5 breakthrough infection sera is comparable between BA.2 and BA.2.75. In this regard, a recent study showed that BA.2.75 exhibits a pronounced resistance to BA.5 breakthrough infection sera compared with BA.2 (Cao et al., 2022). This discrepancy may be explained by the type of vaccine used: a cohort in the present study was vaccinated with mRNA vaccines (BNT162b2 or mRNA-1273), whereas the cohort in the previous study (Cao et al., 2022) was vaccinated with an inactivated vaccine (CoronaVac). In fact, another study on a cohort of mRNA-1273 vaccination showed results consistent with ours (Shen et al., 2022). These observations suggest that the basal immunity induced by vaccination is different by the type of vaccine used, and thereby, the immunity induced by breakthrough BA.5 infection is different.

We showed that G446S in BA.2.75 S was closely associated with resistance to various antisera: 4-dose vaccinated sera, breakthrough BA.5 infection sera, and BA.2- and BA.5-infected hamster sera. Additionally, G446S was responsible for the increased resistance to therapeutic antibodies, such as bebtelovimab and cilgavimab. These results suggest that G446S is critical to evade diverse antibodies. Importantly, our receptor-binding assay showed that G446S significantly decreased the binding affinity of BA.2 RBD to human ACE2, and this effect was compensated by the other substitutions in the BA.2.75 S RBD, particularly by N460K. Altogether, these results suggest that G446S was acquired to evade antiviral immunity, and the other substitutions in the RBD, such as N460K, were acquired likely to compensate for the ACE2 binding affinity reduced by G446S. This is reminiscent of our recent study focusing on Omicron BA.5 (Kimura et al., 2022c): in the case of the BA.5 S, F486V resulted in immune evasion and decreased binding affinity to ACE2, whereas L452R compensated the decreased ACE2 binding affinity. Although the mechanisms of action are different between BA.5 and BA.2.75, the acquisition of two types of substitutions—one leads to immune evasion, which tends to decrease ACE2 affinity, and the other leads to increased ACE2 affinity for compensation—might be a common strategy of SARS-CoV-2 evolution.

Our investigation using viral genome surveillance data reported from India suggested that BA.2.75 has the potential to outcompete BA.2 as well as BA.5, the most predominant variant in the world as of August 2022. Following the worldwide spread of BA.5, it is probable that the number of individuals infected with BA.5 will increase. Additionally, we showed that the intrinsic pathogenicity of BA.2.75 in hamsters is comparable with that of BA.5 and higher than that of BA.2. Since a recent study showed that the hospitalization risk of BA.5 was significantly higher than that of BA.2 in the once-boosted vaccinated population (Kislaya et al., 2022), it is not unreasonable to infer that the intrinsic pathogenicity in infected hamsters reflects the severity and outcome in infected humans to a meaningful extent.

In summary, our multisystem investigations revealed that the growth rate in the human population, fusogenicity, and intrinsic pathogenicity of BA.2.75 are greater than those of BA.2. These features of BA.2.75 suggest the potential risk of this variant to global health. Since BA.2.75 shows significantly higher R_e than BA.2 and BA.5 in India, this variant will probably transmit to and outcompete BA.2 and BA.5 in some countries other than India in the near future. For the assessment of the potential risk of BA.2.75 to global health, this variant should be under monitoring carefully and continuously through worldwide cooperation of in-depth viral genomic surveillance.

CONSORTIA

Mai Kishimoto, Marie Kato, Zannatul Ferdous, Hiromi Mouri, Kenji Shishido, Naoko Misawa, Mai Suganami, Mika Chiba, Ryo Yoshimura, So Nakagawa, Jiaqi Wu, Yasuhiro Kazuma, Ryosuke Nomura, Yoshihito Horisawa, Yusuke Tashiro, Yugo Kawai, Ryoko Kawabata, Otowa Takahashi, Kimiko Ichihara, Chihiro Motozono, Yuri L. Tanaka, Erika P. Butlertanaka, Rina Hashimoto, Tateki Suzuki, Kanako Kimura, Jiei Sasaki, and Yukari Nakajima

STAR★METHODS

Detailed methods are provided in the online version of this paper and include the following:

- KEY RESOURCES TABLE
- RESOURCE AVAILABILITY
  - Lead contact
  - Materials availability
  - Data and code availability
- EXPERIMENTAL MODEL AND SUBJECT DETAILS
  - Ethics statement
  - Human serum collection
  - Cell culture
- METHOD DETAILS
  - Viral genome sequencing
  - Phylogenetic analyses
  - Modeling the epidemic dynamics of SARS-CoV-2 lineages
  - Plasmid construction
  - Preparation of monoclonal antibodies

- Neutralization assay
- Airway organoids
- SARS-CoV-2 preparation and titration
- Antiviral drug assay using SARS-CoV-2 clinical isolates and AOs
- Cytotoxicity assay
- Pseudovirus infection
- Yeast surface display
- Protein expression and purification for cryo-EM
- Cryo-EM sample preparation and data collection
- Cryo-EM image processing
- Cryo-EM model building and analysis
- SARS-CoV-2 S-based fusion assay
- Coculture experiment
- AO-ALI model
- Preparation of human airway and lung epithelial cells from human iPSCs
- Airway-on-a-chips
- Microfluidic device
- SARS-CoV-2 infection
- RT–qPCR
- Plaque assay
- Animal experiments
- Lung function test
- Immunohistochemistry
- H&E staining
- Histopathological scoring

● QUANTIFICATION AND STATISTICAL ANALYSIS

SUPPLEMENTAL INFORMATION

Supplemental information can be found online at https://doi.org/10.1016/j.chom.2022.10.003.

ACKNOWLEDGMENTS

We would like to thank all members belonging to G2P-Japan Consortium. We thank National Institute for Infectious Diseases, Japan, for providing clinical isolates of BA.2.75 and BA.2 and the technical assistance from The Research Support Center, Research Center for Human Disease Modeling, and Kyushu University Graduate School of Medical Sciences. We appreciate all data contributors, i.e., the authors and their originating laboratories responsible for obtaining the specimens, and their submitting laboratories for generating the genetic sequence and metadata and sharing via the GISAID Initiative, on which this research is based. The super-computing resource was provided by Human Genome Center at The University of Tokyo. This study was supported in-part by AMED Program on R&D of new generation vaccine including new modality application (JP223fa727002 to K. Sato); AMED Research Program on Emerging and Re-emerging Infectious Diseases (JP21fk0108574 to H.N.; JP21fk0108465 to A.S.; JP21fk0108493 to T.F.; JP22fk0108617 to T.F.; JP22fk0108146 to K. Sato; JP21fk0108494 to H.F., G2P-Japan Consortium, K. Shirakawa, T. Irie, K. Matsuno, S.T., T. Ikeda, T.F., and K. Sato); AMED CRDF Global Grant (JP22jk0210039 to A.S.); AMED Japan Program for Infectious Diseases Research and Infrastructure (JP22wm0325009 to A.S.; JP22wm0125008 to K. Matsuno); AMED BINDS (JP21am0101093 and JP22ama121037 to K. Maenaka); AMED CREST (JP21gm1610005 to K. Takayama); JST CREST (JPMJCR20H8 to T.H. and H.F.; JPMJCR20H4 to K. Sato); JSPS KAKENHI Scientific Research C (22K07089 to M. Toyoda; 22K07103, to T. Ikeda); JSPS Scientific Research B (21H02736 to T.F.); JSPS Early-Career Scientists (22K16375 to H.N.; 20K15767 to J.I.); JSPS Core-to-Core Program (A. Advanced Research Networks) (JPJSCCA20190008 to T.H. and K. Sato); JSPS Transformative Research Areas B JP20H05773 (to T.H.); JSPS Transformative Research Areas A JP20H05873 (to K. Maenaka); JSPS Research Fellow DC2 (22J11578 to K.U.); JSPS Leading Initiative for Excellent Young Researchers (LEADER) (to T. Ikeda); World-leading Innovative and Smart Education (WISE) Program 1801 from the Ministry of Education, Culture, Sports, Science and Technology (to N.N.); Tokyo Biochemical Research Foundation (to K. Sato); Takeda Science Foundation (to K. Maenaka and T. Ikeda); Naito Foundation (to T.H.); Shin-Nihon Foundation of Advanced Medical Research (to M. Toyoda and T. Ikeda); Waksman Foundation of Japan (to T. Ikeda); Hokkaido University, Global Facility Center, Pharma Science Open Unit (to K. Maenaka); Cooperative Research Program, Institute for Life and Medical Sciences, Kyoto University (to K. Maenaka); an intramural grant from Kumamoto University COVID-19 Research Projects (AMABIE) (to T. Ikeda); and the project of National Institute of Virology and Bacteriology, Programme EXCELES, funded by the European Union, Next Generation EU (LX22NPO5103 to J.Z.).

AUTHOR CONTRIBUTIONS

A.S., S.D., I.K., H.N., M. Toyoda, K.N., K.U., Y.K., S.F., D.Y., M.S., M.M.B., R. Shimizu, T. Irie, T.U., and T. Ikeda performed cell culture experiments. T.T., K. Tabata, R. Suzuki, H.I., N.N., K. Yoshimatsu, H.S., K. Matsuno, and T.F. performed animal experiments. Y.O., L.W., M. Tsuda, and S.T. performed histopathological analysis. J.Z. and G.S. performed yeast surface display assay. Y.A., S.K., K.S.-T., H.F., K. Maenaka, and T.H. performed structural analysis. S.D. and K. Takayama prepared AO, AO-ALI, and airway-on-a-chip systems. Y.Y. and T.N. performed generation and provision of human iPSC-derived airway and alveolar epithelial cells. H.A., M.N., K. Sadamasu, and K. Yoshimura performed viral genome sequencing analysis. J.K., A.T.-K., and K. Shirakawa contributed clinical sample collection. J.I. performed statistical, modeling, and bioinformatics analyses. J.I., K. Takayama, K.M., S.T., T. Ikeda, T.F., and K. Sato designed the experiments and interpreted the results. J.I., T.I., T.F., and K. Sato wrote the original manuscript. All authors reviewed and proofread the manuscript. The Genotype to Phenotype Japan (G2P-Japan) Consortium contributed to the project administration.

DECLARATION OF INTERESTS

Y.Y. and T.N. are founders and shareholders of HiLung, Inc. Y.Y. is a co-inventor of patents (PCT/JP2016/057254; "method for inducing differentiation of alveolar epithelial cells," PCT/JP2016/059786, "method of producing airway epithelial cells").

Received: August 9, 2022
Revised: September 27, 2022
Accepted: October 4, 2022
Published: October 9, 2022

REFERENCES

Adams, P.D., Afonine, P.V., Bunkóczi, G., Chen, V.B., Davis, I.W., Echols, N., Headd, J.J., Hung, L.W., Kapral, G.J., Grosse-Kunstleve, R.W., et al. (2010). Phenix: a comprehensive Python-based system for macromolecular structure solution. Acta Crystallogr. D Biol. Crystallogr. *66*, 213–221. https://doi.org/10.1107/S0907444909052925.

Arora, P., Kempf, A., Nehlmeier, I., Schulz, S.R., Cossmann, A., Stankov, M.V., Jäck, H.M., Behrens, G.M.N., Pöhlmann, S., and Hoffmann, M. (2022). Augmented neutralisation resistance of emerging omicron subvariants BA.2.12.1, BA.4, and BA.5. Lancet Infect. Dis. *22*, 1117–1118. https://doi.org/10.1016/S1473-3099(22)00422-4.

Barnes, C.O., Jette, C.A., Abernathy, M.E., Dam, K.A., Esswein, S.R., Gristick, H.B., Malyutin, A.G., Sharaf, N.G., Huey-Tubman, K.E., Lee, Y.E., et al. (2020). SARS-CoV-2 neutralizing antibody structures inform therapeutic strategies. Nature *588*, 682–687. https://doi.org/10.1038/s41586-020-2852-1.

Bruel, T., Hadjadj, J., Maes, P., Planas, D., Seve, A., Staropoli, I., Guivel-Benhassine, F., Porrot, F., Bolland, W.H., Nguyen, Y., et al. (2022). Serum neutralization of SARS-CoV-2 Omicron sublineages BA.1 and BA.2 in patients receiving monoclonal antibodies. Nat. Med. *28*, 1297–1302. https://doi.org/10.1038/s41591-022-01792-5.

Cao, Y., Song, W., Wang, L., Liu, P., Yue, C., Jian, F., Yu, Y., Yisimayi, A., Wang, P., Wang, Y., et al. (2022). Characterizations of enhanced infectivity and antibody evasion of Omicron BA.2.75. Preprint at bioRxiv. https://doi.org/10.1101/2022.07.18.500332.

Cao, Y., Wang, J., Jian, F., Xiao, T., Song, W., Yisimayi, A., Huang, W., Li, Q., Wang, P., An, R., et al. (2021). Omicron escapes the majority of existing SARS-CoV-2 neutralizing antibodies. Preprint at bioRxiv. https://doi.org/10.1101/2021.12.07.470392.

Cao, Y., Yisimayi, A., Jian, F., Song, W., Xiao, T., Wang, L., Du, S., Wang, J., Li, Q., Chen, X., et al. (2022). BA.2.12.1, BA.4 and BA.5 escape antibodies elicited by Omicron infection. Nature *608*, 593–602. https://doi.org/10.1038/s41586-022-04980-y.

Capella-Gutiérrez, S., Silla-Martínez, J.M., and Gabaldón, T. (2009). trimAl: a tool for automated alignment trimming in large-scale phylogenetic analyses. Bioinformatics *25*, 1972–1973. https://doi.org/10.1093/bioinformatics/btp348.

Cardone, G., Heymann, J.B., and Steven, A.C. (2013). One number does not fit all: mapping local variations in resolution in cryo-EM reconstructions. J. Struct. Biol. *184*, 226–236. https://doi.org/10.1016/j.jsb.2013.08.002.

Cele, S., Jackson, L., Khoury, D.S., Khan, K., Moyo-Gwete, T., Tegally, H., San, J.E., Cromer, D., Scheepers, C., Amoako, D.G., et al. (2021). Omicron extensively but incompletely escapes Pfizer BNT162b2 neutralization. Nature *602*, 654–656. https://doi.org/10.1038/d41586-41021-03824-41585.

Cerutti, G., Guo, Y., Zhou, T., Gorman, J., Lee, M., Rapp, M., Reddem, E.R., Yu, J., Bahna, F., Bimela, J., et al. (2021). Potent SARS-CoV-2 neutralizing antibodies directed against spike N-terminal domain target a single Supersite. Cell Host Microbe *29*, 819–833.e7. https://doi.org/10.1016/j.chom.2021.03.005.

Chan, K.K., Dorosky, D., Sharma, P., Abbasi, S.A., Dye, J.M., Kranz, D.M., Herbert, A.S., and Procko, E. (2020). Engineering human ACE2 to optimize binding to the spike protein of SARS coronavirus 2. Science *369*, 1261–1265. https://doi.org/10.1126/science.abc0870.

Chen, S., Zhou, Y., Chen, Y., and Gu, J. (2018). fastp: an ultra-fast all-in-one FASTQ preprocessor. Bioinformatics *34*, i884–i890. https://doi.org/10.1093/bioinformatics/bty560.

Chi, X., Yan, R., Zhang, J., Zhang, G., Zhang, Y., Hao, M., Zhang, Z., Fan, P., Dong, Y., Yang, Y., et al. (2020). A neutralizing human antibody binds to the N-terminal domain of the Spike protein of SARS-CoV-2. Science *369*, 650–655. https://doi.org/10.1126/science.abc6952.

Cingolani, P., Platts, A., Wang, L.L., Coon, M., Nguyen, T., Wang, L., Land, S.J., Lu, X., and Ruden, D.M. (2012). A program for annotating and predicting the effects of single nucleotide polymorphisms, SnpEff: SNPs in the genome of Drosophila melanogaster strain w1118; iso-2; iso-3. Fly (Austin) *6*, 80–92. https://doi.org/10.4161/fly.19695.

Deguchi, S., Tsuda, M., Kosugi, K., Sakamoto, A., Mimura, N., Negoro, R., Sano, E., Nobe, T., Maeda, K., Kusuhara, H., et al. (2021). Usability of polydimethylsiloxane-based microfluidic devices in pharmaceutical research using human hepatocytes. ACS Biomater. Sci. Eng. *7*, 3648–3657. https://doi.org/10.1021/acsbiomaterials.1c00642.

Dejnirattisai, W., Huo, J., Zhou, D., Zahradník, J., Supasa, P., Liu, C., Duyvesteyn, H.M.E., Ginn, H.M., Mentzer, A.J., Tuekprakhon, A., et al. (2022). SARS-CoV-2 Omicron-B.1.1.529 leads to widespread escape from neutralizing antibody responses. Cell *185*, 467–484.e15. https://doi.org/10.1016/j.cell.2021.12.046.

Dong, J., Zost, S.J., Greaney, A.J., Starr, T.N., Dingens, A.S., Chen, E.C., Chen, R.E., Case, J.B., Sutton, R.E., Gilchuk, P., et al. (2021). Genetic and structural basis for SARS-CoV-2 variant neutralization by a two-antibody cocktail. Nat. Microbiol. *6*, 1233–1244. https://doi.org/10.1038/s41564-021-00972-2.

Emsley, P., and Cowtan, K. (2004). Coot: model-building tools for molecular graphics. Acta Crystallogr. D Biol. Crystallogr. *60*, 2126–2132. https://doi.org/10.1107/S0907444904019158.

Ferreira, I.A.T.M., Kemp, S.A., Datir, R., Saito, A., Meng, B., Rakshit, P., Takaori-Kondo, A., Kosugi, Y., Uriu, K., Kimura, I., et al. (2021). SARS-CoV-2 B.1.617 Mutations L452R and E484Q Are Not Synergistic for Antibody Evasion. J. Infect. Dis. *224*, 989–994. https://doi.org/10.1093/infdis/jiab368.

Garcia-Beltran, W.F., Lam, E.C., St. Denis, K., Nitido, A.D., Garcia, Z.H., Hauser, B.M., Feldman, J., Pavlovic, M.N., Gregory, D.J., Poznansky, M.C., et al. (2021). Multiple SARS-CoV-2 variants escape neutralization by vaccine-induced humoral immunity. Cell *184*, 2372–2383.e9. https://doi.org/10.1016/j.cell.2021.03.013.

GitHub (2022). BA.2 sublineage with S:K147E, W152R, F157L, I210V, G257S, D339H, G446S, N460K, R493Q (73 seq as of 2022-06-29, mainly India) (June 21, 2022). https://github.com/cov-lineages/pango-designation/issues/773.

Goddard, T.D., Huang, C.C., Meng, E.C., Pettersen, E.F., Couch, G.S., Morris, J.H., and Ferrin, T.E. (2018). UCSF ChimeraX: meeting modern challenges in visualization and analysis. Protein Sci. *27*, 14–25. https://doi.org/10.1002/pro.3235.

Gotoh, S., Ito, I., Nagasaki, T., Yamamoto, Y., Konishi, S., Korogi, Y., Matsumoto, H., Muro, S., Hirai, T., Funato, M., et al. (2014). Generation of alveolar epithelial spheroids via isolated progenitor cells from human pluripotent stem cells. Stem Cell Rep. *3*, 394–403. https://doi.org/10.1016/j.stemcr.2014.07.005.

Gruell, H., Vanshylla, K., Korenkov, M., Tober-Lau, P., Zehner, M., Münn, F., Janicki, H., Augustin, M., Schommers, P., Sander, L.E., et al. (2022). SARS-CoV-2 Omicron sublineages exhibit distinct antibody escape patterns. Cell Host Microbe *30*, 1231–1241.e6. https://doi.org/10.1016/j.chom.2022.07.002.

Hachmann, N.P., Miller, J., Collier, A.Y., Ventura, J.D., Yu, J., Rowe, M., Bondzie, E.A., Powers, O., Surve, N., Hall, K., et al. (2022). Neutralization escape by SARS-CoV-2 Omicron subvariants BA.2.12.1, BA.4, and BA.5. N. Engl. J. Med. *387*, 86–88. https://doi.org/10.1056/NEJMc2206576.

Harvey, W.T., Carabelli, A.M., Jackson, B., Gupta, R.K., Thomson, E.C., Harrison, E.M., Ludden, C., Reeve, R., Rambaut, A., et al.; COVID-19 Genomics UK (COG-UK) Consortium (2021). SARS-CoV-2 variants, spike mutations and immune escape. Nat. Rev. Microbiol. *19*, 409–424. https://doi.org/10.1038/s41579-021-00573-0.

Hashiguchi, T., Ose, T., Kubota, M., Maita, N., Kamishikiryo, J., Maenaka, K., and Yanagi, Y. (2011). Structure of the measles virus hemagglutinin bound to its cellular receptor SLAM. Nat. Struct. Mol. Biol. *18*, 135–141. https://doi.org/10.1038/nsmb.1969.

Hashimoto, R., Takahashi, J., Shirakura, K., Funatsu, R., Kosugi, K., Deguchi, S., Yamamoto, M., Tsunoda, Y., Morita, M., Muraoka, K., et al. (2022). SARS-CoV-2 disrupts the respiratory vascular barrier by suppressing Claudin-5 expression. Sci. Adv. *8*, eabo6783. https://doi.org/10.1126/sciadv.abo6783.

Hsieh, C.L., Goldsmith, J.A., Schaub, J.M., DiVenere, A.M., Kuo, H.C., Javanmardi, K., Le, K.C., Wrapp, D., Lee, A.G., Liu, Y., et al. (2020). Structure-based design of prefusion-stabilized SARS-CoV-2 spikes. Science *369*, 1501–1505. https://doi.org/10.1126/science.abd0826.

Jackson, C.B., Farzan, M., Chen, B., and Choe, H. (2022). Mechanisms of SARS-CoV-2 entry into cells. Nat. Rev. Mol. Cell Biol. *23*, 3–20. https://doi.org/10.1038/s41580-021-00418-x.

Jurrus, E., Engel, D., Star, K., Monson, K., Brandi, J., Felberg, L.E., Brookes, D.H., Wilson, L., Chen, J., Liles, K., et al. (2018). Improvements to the APBS biomolecular solvation software suite. Protein Sci. *27*, 112–128. https://doi.org/10.1002/pro.3280.

Khan, K., Karim, F., Ganga, Y., Bernstein, M., Jule, Z., Reedoy, K., Cele, S., Lustig, G., Amoako, D., Wolter, N., et al. (2022). Omicron sub-lineages BA.4/BA.5 escape BA.1 infection elicited neutralizing immunity. Preprint at medRxiv. https://doi.org/10.1101/2022.1104.1129.22274477.

Khare, S., Gurry, C., Freitas, L., Schultz, M.B., Bach, G., Diallo, A., Akite, N., Ho, J., Lee, R.T., Yeo, W., et al. (2021). GISAID's role in pandemic response. China CDC Wkly. *3*, 1049–1051. https://doi.org/10.46234/ccdcw2021.255.

Kim, C., Ryu, D.K., Lee, J., Kim, Y.I., Seo, J.M., Kim, Y.G., Jeong, J.H., Kim, M., Kim, J.I., Kim, P., et al. (2021). A therapeutic neutralizing antibody targeting receptor binding domain of SARS-CoV-2 spike protein. Nat. Commun. *12*, 288. https://doi.org/10.1038/s41467-020-20602-5.

Kimura, I., Kosugi, Y., Wu, J., Zahradnik, J., Yamasoba, D., Butlertanaka, E.P., Tanaka, Y.L., Uriu, K., Liu, Y., Morizako, N., et al. (2022a). The SARS-CoV-2

Lambda variant exhibits enhanced infectivity and immune resistance. Cell Rep. *38*, 110218. https://doi.org/10.1016/j.celrep.2021.110218.

Kimura, I., Yamasoba, D., Nasser, H., Zahradnik, J., Kosugi, Y., Wu, J., Nagata, K., Uriu, K., Tanaka, Y.L., Ito, J., et al. (2022b). SARS-CoV-2 spike S375F mutation characterizes the Omicron BA.1 variant. Preprint at bioRxiv. https://doi.org/10.1101/2022.1104.1103.486864.

Kimura, I., Yamasoba, D., Tamura, T., Nao, N., Suzuki, T., Oda, Y., Mitoma, S., Ito, J., Nasser, H., Zahradnik, J., et al. (2022c). Virological characteristics of the novel SARS-CoV-2 Omicron variants including BA.4 and BA.5. Cell *185*, 2103–2115.e19. https://doi.org/10.1016/j.cell.2022.1009.1018.

Kislaya, I., Casaca, P., Borges, V., et al. (2022). SARS-CoV-2 BA.5 vaccine breakthrough risk and severity compared with BA.2: a case-case and cohort study using electronic health records in Portugal. Preprint at medRxiv. https://doi.org/10.1101/2022.1107.1125.22277996.

Kondo, N., Miyauchi, K., and Matsuda, Z. (2011). Monitoring viral-mediated membrane fusion using fluorescent reporter methods. Curr. Protoc. Cell Biol. *Chapter*. Unit 26.9. https://doi.org/10.1002/0471143030.cb2609s50.

Konishi, S., Gotoh, S., Tateishi, K., Yamamoto, Y., Korogi, Y., Nagasaki, T., Matsumoto, H., Muro, S., Hirai, T., Ito, I., et al. (2016). Directed induction of functional multi-ciliated cells in proximal airway epithelial spheroids from human pluripotent stem cells. Stem Cell Rep. *6*, 18–25. https://doi.org/10.1016/j.stemcr.2015.11.010.

Lan, J., Ge, J., Yu, J., Shan, S., Zhou, H., Fan, S., Zhang, Q., Shi, X., Wang, Q., Zhang, L., et al. (2020). Structure of the SARS-CoV-2 spike receptor-binding domain bound to the ACE2 receptor. Nature *581*, 215–220. https://doi.org/10.1038/s41586-020-2180-5.

Li, H. (2018). Minimap2: pairwise alignment for nucleotide sequences. Bioinformatics *34*, 3094–3100. https://doi.org/10.1093/bioinformatics/bty191.

Li, H., and Durbin, R. (2009). Fast and accurate short read alignment with Burrows-Wheeler transform. Bioinformatics *25*, 1754–1760. https://doi.org/10.1093/bioinformatics/btp324.

Li, H., Handsaker, B., Wysoker, A., Fennell, T., Ruan, J., Homer, N., Marth, G., Abecasis, G., and Durbin, R.; 1000 Genome Project Data Processing Subgroup (2009). The sequence alignment/map format and SAMtools. Bioinformatics *25*, 2078–2079. https://doi.org/10.1093/bioinformatics/btp352.

Liu, L., Iketani, S., Guo, Y., Chan, J.F., Wang, M., Liu, L., Luo, Y., Chu, H., Huang, Y., Nair, M.S., et al. (2021). Striking antibody evasion manifested by the Omicron variant of SARS-CoV-2. Nature *602*, 676–681. https://doi.org/10.1038/d41586-41021-03826-41583.

Liu, L., Wang, P., Nair, M.S., Yu, J., Rapp, M., Wang, Q., Luo, Y., Chan, J.F., Sahi, V., Figueroa, A., et al. (2020). Potent neutralizing antibodies against multiple epitopes on SARS-CoV-2 spike. Nature *584*, 450–456. https://doi.org/10.1038/s41586-020-2571-7.

Liu, Y., Arase, N., Kishikawa, J.-i., Hirose, M., Li, S., Tada, A., Matsuoka, S., Arakawa, A., Akamatsu, K., Ono, C., et al. (2021). The SARS-CoV-2 Delta variant is poised to acquire complete resistance to wild-type spike vaccines. Preprint at bioRxiv. https://doi.org/10.1101/2021.1108.1122.457114.

Lok, S.M. (2021). An NTD Supersite of attack. Cell Host Microbe *29*, 744–746. https://doi.org/10.1016/j.chom.2021.04.010.

Lyke, K.E., Atmar, R.L., Islas, C.D., Posavad, C.M., Szydlo, D., Paul Chourdhury, R., Deming, M.E., Eaton, A., Jackson, L.A., Branche, A.R., et al. (2022). Rapid decline in vaccine-boosted neutralizing antibodies against SARS-CoV-2 Omicron variant. Cell Rep. Med. *3*, 100679. https://doi.org/10.1016/j.xcrm.2022.100679.

Matsuyama, S., Nao, N., Shirato, K., Kawase, M., Saito, S., Takayama, I., Nagata, N., Sekizuka, T., Katoh, H., Kato, F., et al. (2020). Enhanced isolation of SARS-CoV-2 by TMPRSS2-expressing cells. Proc. Natl. Acad. Sci. USA *117*, 7001–7003. https://doi.org/10.1073/pnas.2002589117.

McCallum, M., De Marco, A., Lempp, F.A., Tortorici, M.A., Pinto, D., Walls, A.C., Beltramello, M., Chen, A., Liu, Z., Zatta, F., et al. (2021). N-terminal domain antigenic mapping reveals a site of vulnerability for SARS-CoV-2. Cell *184*, 2332–2347.e16. https://doi.org/10.1016/j.cell.2021.03.028.

Meng, B., Abdullahi, A., Ferreira, I.A.T.M., Goonawardane, N., Saito, A., Kimura, I., Yamasoba, D., Gerber, P.P., Fatihi, S., Rathore, S., et al. (2022). Altered TMPRSS2 usage by SARS-CoV-2 Omicron impacts tropism and fusogenicity. Nature *603*, 706–714. https://doi.org/10.1038/s41586-022-04474-x.

Mirdita, M., Schütze, K., Moriwaki, Y., Heo, L., Ovchinnikov, S., and Steinegger, M. (2022). ColabFold: making protein folding accessible to all. Nat. Methods *19*, 679–682. https://doi.org/10.1038/s41592-022-01488-1.

Mittal, A., Khattri, A., and Verma, V. (2022). Structural and antigenic variations in the spike protein of emerging SARS-CoV-2 variants. PLOS Pathog. *18*. e1010260. https://doi.org/10.1371/journal.ppat.1010260.

Motozono, C., Toyoda, M., Zahradnik, J., Saito, A., Nasser, H., Tan, T.S., Ngare, I., Kimura, I., Uriu, K., Kosugi, Y., et al. (2021). SARS-CoV-2 spike L452R variant evades cellular immunity and increases infectivity. Cell Host Microbe *29*, 1124–1136.e11. https://doi.org/10.1016/j.chom.2021.06.006.

Niwa, H., Yamamura, K., and Miyazaki, J. (1991). Efficient selection for high-expression transfectants with a novel eukaryotic vector. Gene *108*, 193–199. https://doi.org/10.1016/0378-1119(91)90434-d.

Ozono, S., Zhang, Y., Ode, H., Sano, K., Tan, T.S., Imai, K., Miyoshi, K., Kishigami, S., Ueno, T., Iwatani, Y., et al. (2021). SARS-CoV-2 D614G spike mutation increases entry efficiency with enhanced ACE2-binding affinity. Nat. Commun. *12*, 848. https://doi.org/10.1038/s41467-021-21118-2.

Ozono, S., Zhang, Y., Tobiume, M., Kishigami, S., and Tokunaga, K. (2020). Super-rapid quantitation of the production of HIV-1 harboring a luminescent peptide tag. J. Biol. Chem. *295*, 13023–13030. https://doi.org/10.1074/jbc.RA120.013887.

Pettersen, E.F., Goddard, T.D., Huang, C.C., Couch, G.S., Greenblatt, D.M., Meng, E.C., and Ferrin, T.E. (2004). UCSF Chimera—a visualization system for exploratory research and analysis. J. Comput. Chem. *25*, 1605–1612. https://doi.org/10.1002/jcc.20084.

Pinto, D., Park, Y.J., Beltramello, M., Walls, A.C., Tortorici, M.A., Bianchi, S., Jaconi, S., Culap, K., Zatta, F., De Marco, A., et al. (2020). Cross-neutralization of SARS-CoV-2 by a human monoclonal SARS-CoV antibody. Nature *583*, 290–295. https://doi.org/10.1038/s41586-020-2349-y.

Planas, D., Saunders, N., Maes, P., Guivel-Benhassine, F., Planchais, C., Buchrieser, J., Bolland, W.H., Porrot, F., Staropoli, I., Lemoine, F., et al. (2021). Considerable escape of SARS-CoV-2 Omicron to antibody neutralization. Nature *602*, 671–675. https://doi.org/10.1038/d41586-41021-03827-41582.

Punjani, A., Rubinstein, J.L., Fleet, D.J., and Brubaker, M.A. (2017). cryoSPARC: algorithms for rapid unsupervised cryo-EM structure determination. Nat. Methods *14*, 290–296. https://doi.org/10.1038/nmeth.4169.

Qu, P., Faraone, J., Evans, J.P., Zou, X., Zheng, Y.M., Carlin, C., Bednash, J.S., Lozanski, G., Mallampalli, R.K., Saif, L.J., et al. (2022). Neutralization of the SARS-CoV-2 omicron BA.4/5 and BA.2.12.1 Subvariants. N. Engl. J. Med. *386*, 2526–2528. https://doi.org/10.1056/NEJMc2206725.

Reed, L.J., and Muench, H. (1938). A simple method of estimating fifty percent endpoints. Am. J. Hyg. *27*, 493–497.

Reeves, P.J., Callewaert, N., Contreras, R., and Khorana, H.G. (2002). Structure and function in rhodopsin: high-level expression of rhodopsin with restricted and homogeneous N-glycosylation by a tetracycline-inducible N-acetylglucosaminyltransferase I-negative HEK293S stable mammalian cell line. Proc. Natl. Acad. Sci. USA *99*, 13419–13424. https://doi.org/10.1073/pnas.212519299.

Saito, A., Irie, T., Suzuki, R., Maemura, T., Nasser, H., Uriu, K., Kosugi, Y., Shirakawa, K., Sadamasu, K., Kimura, I., et al. (2022). Enhanced fusogenicity and pathogenicity of SARS-CoV-2 Delta P681R mutation. Nature *602*, 300–306. https://doi.org/10.1038/s41586-021-04266-9.

Sano, E., Suzuki, T., Hashimoto, R., Itoh, Y., Sakamoto, A., Sakai, Y., Saito, A., Okuzaki, D., Motooka, D., Muramoto, Y., et al. (2022). Cell response analysis in SARS-CoV-2 infected bronchial organoids. Commun. Biol. *5*, 516. https://doi.org/10.1038/s42003-022-03499-2.

Shen, X., Chalkias, S., Feng, J., Chen, X., Zhou, H., Marshall, J.C., Girard, B., Tomassini, J.E., Aunins, A., Das, R., et al. (2022). Neutralization of

SARS-CoV-2 omicron BA.2.75 after mRNA-1273 Vaccination. N. Engl. J. Med. *387*, 1234–1236. https://doi.org/10.1056/NEJMc2210648.

Stalls, V., Lindenberger, J., Gobeil, S.M., Henderson, R., Parks, R., Barr, M., Deyton, M., Martin, M., Janowska, K., Huang, X., et al. (2022). Cryo-EM structures of SARS-CoV-2 Omicron BA.2 spike. Cell Rep. *39*, 111009. https://doi.org/10.1016/j.celrep.2022.111009.

Stamatakis, A. (2014). RAxML version 8: a tool for phylogenetic analysis and post-analysis of large phylogenies. Bioinformatics *30*, 1312–1313. https://doi.org/10.1093/bioinformatics/btu033.

Suryadevara, N., Shrihari, S., Gilchuk, P., VanBlargan, L.A., Binshtein, E., Zost, S.J., Nargi, R.S., Sutton, R.E., Winkler, E.S., Chen, E.C., et al. (2021). Neutralizing and protective human monoclonal antibodies recognizing the N-terminal domain of the SARS-CoV-2 spike protein. Cell *184*, 2316–2331.e15. https://doi.org/10.1016/j.cell.2021.03.029.

Suzuki, R., Yamasoba, D., Kimura, I., Wang, L., Kishimoto, M., Ito, J., Morioka, Y., Nao, N., Nasser, H., Uriu, K., et al. (2022). Attenuated fusogenicity and pathogenicity of SARS-CoV-2 Omicron variant. Nature *603*, 700–705. https://doi.org/10.1038/s41586-022-04462-1.

Takashita, E., Kinoshita, N., Yamayoshi, S., Sakai-Tagawa, Y., Fujisaki, S., Ito, M., Iwatsuki-Horimoto, K., Chiba, S., Halfmann, P., Nagai, H., et al. (2022). Efficacy of antibodies and antiviral drugs against Covid-19 Omicron variant. N. Engl. J. Med. *386*, 995–998. https://doi.org/10.1056/NEJMc2119407.

Takashita, E., Kinoshita, N., Yamayoshi, S., Sakai-Tagawa, Y., Fujisaki, S., Ito, M., Iwatsuki-Horimoto, K., Halfmann, P., Watanabe, S., Maeda, K., et al. (2022). Efficacy of antiviral agents against the SARS-CoV-2 Omicron subvariant BA.2. N. Engl. J. Med. *386*, 1475–1477. https://doi.org/10.1056/NEJMc2201933.

Tamura, T., Yamasoba, D., Oda, Y., Ito, J., Kamasaki, T., Nao, N., Hashimoto, R., Fujioka, Y., Suzuki, R., Wang, L., et al. (2022). Comparative pathogenicity of SARS-CoV-2 Omicron subvariants including BA.1, BA.2, and BA.5. Preprint at bioRxiv. https://doi.org/10.1101/2022.1108.1105.502758.

Tuekprakhon, A., Nutalai, R., Dijokaite-Guraliuc, A., Zhou, D., Ginn, H.M., Selvaraj, M., Liu, C., Mentzer, A.J., Supasa, P., Duyvesteyn, H.M.E., et al. (2022). Antibody escape of SARS-CoV-2 Omicron BA.4 and BA.5 from vaccine and BA.1 serum. Cell *185*, 2422–2433.e13. https://doi.org/10.1016/j.cell.2022.06.005.

Uriu, K., Cárdenas, P., Muñoz, E., Barragan, V., Kosugi, Y., Shirakawa, K., Takaori-Kondo, A.; Ecuador-COVID19 Consortium, The Genotype to Phenotype Japan (G2P-Japan) Consortium, and Sato, K. (2022). Characterization of the immune resistance of SARS-CoV-2 Mu variant and the robust immunity induced by Mu infection. J. Infect. Dis. *226*, 1200–1203. https://doi.org/10.1093/infdis/jiac053.

Uriu, K., Kimura, I., Shirakawa, K., Takaori-Kondo, A., Nakada, T.A., Kaneda, A., Nakagawa, S., and Sato, K.; Genotype to Phenotype Japan (G2P-Japan) Consortium (2021). Neutralization of the SARS-CoV-2 Mu variant by convalescent and vaccine serum. N. Engl. J. Med. *385*, 2397–2399. https://doi.org/10.1056/NEJMc2114706.

VanBlargan, L.A., Errico, J.M., Halfmann, P.J., Zost, S.J., Crowe, J.E., Purcell, L.A., Kawaoka, Y., Corti, D., Fremont, D.H., and Diamond, M.S. (2022). An infectious SARS-CoV-2 B.1.1.529 Omicron virus escapes neutralization by therapeutic monoclonal antibodies. Nat. Med. *28*, 490–495. https://doi.org/10.1038/s41591-021-01678-y.

Voss, W.N., Hou, Y.J., Johnson, N.V., Delidakis, G., Kim, J.E., Javanmardi, K., Horton, A.P., Bartzoka, F., Paresi, C.J., Tanno, Y., et al. (2021). Prevalent, protective, and convergent IgG recognition of SARS-CoV-2 non-RBD spike epitopes. Science *372*, 1108–1112. https://doi.org/10.1126/science.abg5268.

Wang, Q., Guo, Y., Iketani, S., Nair, M.S., Li, Z., Mohri, H., Wang, M., Yu, J., Bowen, A.D., Chang, J.Y., et al. (2022). Antibody evasion by SARS-CoV-2 Omicron subvariants BA.2.12.1, BA.4 and BA.5, & BA.5. Nature *608*, 603–608. https://doi.org/10.1038/s41586-022-05053-w.

Westendorf, K., Žentelis, S., Wang, L., Foster, D., Vaillancourt, P., Wiggin, M., Lovett, E., van der Lee, R., Hendle, J., Pustilnik, A., et al. (2022). LY-CoV1404 (bebtelovimab) potently neutralizes SARS-CoV-2 variants. Cell Rep. *39*, 110812. https://doi.org/10.1016/j.celrep.2022.110812.

WHO (2022). Tracking SARS-CoV-2 variants (July 19, 2022). https://www.who.int/en/activities/tracking-SARS-CoV-2-variants.

Williams, C.J., Headd, J.J., Moriarty, N.W., Prisant, M.G., Videau, L.L., Deis, L.N., Verma, V., Keedy, D.A., Hintze, B.J., Chen, V.B., et al. (2018). MolProbity: more and better reference data for improved all-atom structure validation. Protein Sci. *27*, 293–315. https://doi.org/10.1002/pro.3330.

Xiao, T., Lu, J., Zhang, J., Johnson, R.I., McKay, L.G.A., Storm, N., Lavine, C.L., Peng, H., Cai, Y., Rits-Volloch, S., et al. (2021). A trimeric human angiotensin-converting enzyme 2 as an anti-SARS-CoV-2 agent. Nat. Struct. Mol. Biol. *28*, 202–209. https://doi.org/10.1038/s41594-020-00549-3.

Yamamoto, M., Kiso, M., Sakai-Tagawa, Y., Iwatsuki-Horimoto, K., Imai, M., Takeda, M., Kinoshita, N., Ohmagari, N., Gohda, J., Semba, K., et al. (2020). The anticoagulant nafamostat potently inhibits SARS-CoV-2 S protein-mediated fusion in a cell fusion assay system and viral infection *in vitro* in a cell-yype-dependent manner. Viruses *12*, 629. https://doi.org/10.3390/v12060629.

Yamamoto, Y., Gotoh, S., Korogi, Y., Seki, M., Konishi, S., Ikeo, S., Sone, N., Nagasaki, T., Matsumoto, H., Muro, S., et al. (2017). Long-term expansion of alveolar stem cells derived from human iPS cells in organoids. Nat. Methods *14*, 1097–1106. https://doi.org/10.1038/nmeth.4448.

Yamasoba, D., Kimura, I., Nasser, H., Morioka, Y., Nao, N., Ito, J., Uriu, K., Tsuda, M., Zahradnik, J., Shirakawa, K., et al. (2022a). Virological characteristics of the SARS-CoV-2 Omicron BA.2 spike. Cell *185*, 2103–2115.e19. https://doi.org/10.1016/j.cell.2022.04.035.

Yamasoba, D., Kosugi, Y., Kimura, I., Fujita, S., Uriu, K., Ito, J., and Sato, K.; Genotype to Phenotype Japan (G2P-Japan) Consortium (2022b). Neutralisation sensitivity of SARS-CoV-2 omicron subvariants to therapeutic monoclonal antibodies. Lancet Infect. Dis. *22*, 942–943. https://doi.org/10.1016/S1473-3099(22)00365-6.

Zahradník, J., Dey, D., Marciano, S., Kolářová, L., Charendoff, C.I., Subtil, A., and Schreiber, G. (2021a). A protein-engineered, enhanced yeast display platform for rapid evolution of challenging targets. ACS Synth. Biol. *10*, 3445–3460. https://doi.org/10.1021/acssynbio.1c00395.

Zahradník, J., Marciano, S., Shemesh, M., Zoler, E., Harari, D., Chiaravalli, J., Meyer, B., Rudich, Y., Li, C., Marton, I., et al. (2021b). SARS-CoV-2 variant prediction and antiviral drug design are enabled by RBD in vitro evolution. Nat. Microbiol. *6*, 1188–1198. https://doi.org/10.1038/s41564-021-00954-4.

Please cite this article in press as: Saito et al., Virological characteristics of the SARS-CoV-2 Omicron BA.2.75 variant, Cell Host & Microbe (2022), https://doi.org/10.1016/j.chom.2022.10.003

CellPress
OPEN ACCESS

STAR★METHODS

KEY RESOURCES TABLE

REAGENT or RESOURCE	SOURCE	IDENTIFIER
Antibodies		
Adintrevimab	This study	N/A
Bamlanivimab	Yamasoba et al., 2022b	N/A
Bebtelovimab	Yamasoba et al., 2022b	N/A
Casirivimab	Yamasoba et al., 2022b	N/A
Cilgavimab	Yamasoba et al., 2022b	N/A
Etesevimab	Yamasoba et al., 2022b	N/A
Imdevimab	Yamasoba et al., 2022b	N/A
Regdanvimab	This study	N/A
Sotrovimab	Yamasoba et al., 2022b	N/A
Tixagevimab	Yamasoba et al., 2022b	N/A
Rabbit anti-SARS-CoV-2 S S1/S2 polyclonal antibody	Thermo Fisher Scientific	Cat# PA5-112048; RRID: AB_2866784
Normal rabbit IgG	Southern Biotech	Cat# 0111-01; RRID: AB_2732899
APC-conjugated goat anti-rabbit IgG polyclonal antibody	Jackson ImmunoResearch	Cat# 111-136-144; RRID: AB_2337987
Bacterial and virus strains		
SARS-CoV-2 B.1.1 (strain TKYE610670)	Saito et al., 2022; Suzuki et al., 2022	N/A
SARS-CoV-2 Delta (strain TKYTK1734)	Saito et al., 2022; Suzuki et al., 2022	N/A
SARS-CoV-2 BA.2 (strain TY40-385)	Kimura et al., 2022b; Tamura et al., 2022	N/A
SARS-CoV-2 BA.5 (strain TKYS14631)	Kimura et al., 2022b; Tamura et al., 2022	N/A
SARS-CoV-2 BA.2.75 (strain TY41-716)	This study	N/A
Biological samples		
Human sera	This study	N/A
Human airway epithelial cells derived from human iPSCs	Yamamoto et al., 2017	N/A
Human alveolar epithelial cells derived from human iPSCs	Yamamoto et al., 2017	N/A
Human airway organoids	Sano et al., 2022	N/A
Airway-on-a-chips	Hashimoto et al., 2022	N/A
Chemicals, peptides, and recombinant proteins		
TransIT-LT1	Takara	Cat# MIR2300
Recombinant RNase inhibitor	Takara	Cat# 2313B
Carboxymethyl cellulose	Wako	Cat# 039-01335
4% Paraformaldehyde in PBS	Nacalai Tesque	Cat# 09154-85
Methylene blue	Nacalai Tesque	Cat# 22412-14
Fetal bovine serum	Sigma-Aldrich	Cat# 172012-500ML
Poly-L-lysine	Sigma	Cat# P4832
Hoechst 33342	Thermo Fisher Scientific	Cat# H3570
Fluoromount-G	Southern Biotech	Cat# 0100-01
Penicillin-streptomycin	Sigma-Aldrich	Cat# P4333-100ML
DMEM (high glucose)	Sigma-Aldrich	Cat# 6429-500ML
DMEM (high glucose)	Nacalai Tesque	Cat# 08458-16

(*Continued on next page*)

Please cite this article in press as: Saito et al., Virological characteristics of the SARS-CoV-2 Omicron BA.2.75 variant, Cell Host & Microbe (2022), https://doi.org/10.1016/j.chom.2022.10.003

Continued

REAGENT or RESOURCE	SOURCE	IDENTIFIER
DMEM (low glucose)	Wako	Cat# 041-29775
EMEM	Sigma-Aldrich	Cat# M4655-500ML
EMEM	Wako	Cat# 056-08385
EGM-2-MV medium	Lonza	Cat# CC-3202
SD-CAA medium	Zahradník et al., 2021a	N/A
1/9 medium	Zahradník et al., 2021a	N/A
Glucose	Sigma-Aldrich	Cat# G8270
Galactose	Sigma-Aldrich	Cat# G0750
Yeast nitrogen base	Sigma-Aldrich	Cat# Y0626
Casamino acids	Sigma-Aldrich	Cat# 2240
Sodium phosphate dibasic	Sigma-Aldrich	Cat# S9763
Sodium phosphate monobasic	Sigma-Aldrich	Cat# S3139
PneumaCult ALI medium	STEMCELL Technologies	Cat# ST-05001
Heparin	Nacalai Tesque	Cat# 17513-96
Y-27632	LC Laboratories	Cat# Y-5301
Hydrocortisone	Sigma-Aldrich	Cat# H0135
Puromycin	InvivoGen	Cat# ant-pr-1
Hygromycin	Nacalai Tesque	Cat# 09287-84
G418	Nacalai Tesque	Cat# G8168-10ML
KpnI	New England Biolab	Cat# R0142S
NotI	New England Biolab	Cat# R1089S
PEI Max	Polysciences	Cat# 24765-1
Fibronectin	Sigma-Aldrich	Cat# F1141
Opti-MEM	Thermo Fisher Scientific	Cat# 11058021
Triton X-100	Nacalai Tesque	Cat# 35501-15
EnduRen live cell substrate	Promega	Cat# E6481
Hoechst 33342	Thermo Fisher Scientific	Cat# H3570
Fluoromount-G	SouthernBiotech	Cat# 0100-01
Dexamethasone	Sigma-Aldrich	Cat# D4902
KGF	PeproTech	Cat# 100-19
8-Br-cAMP	Biolog	Cat# B007
3-Isobutyl 1-methylxanthine (IBMX)	Wako	Cat# 095-03413
CHIR99021	Axon Medchem	Cat# 1386
SB431542	Wako	Cat# 198-16543
Soluble human ACE2 (residues 18-618 for binding assay)	Yamasoba et al., 2022b	N/A
Soluble human ACE2 (residues 19-617 for structural analysis)	Yamasoba et al., 2022b	N/A
SARS-CoV-2 B.1.1 RBD	Kimura et al., 2022a; Motozono et al., 2021	N/A
SARS-CoV-2 BA.1 RBD	This study	N/A
SARS-CoV-2 BA.2 RBD	This study	N/A
SARS-CoV-2 BA.5 RBD	This study	N/A
SARS-CoV-2 BA.2.75 RBD	This study	N/A
SARS-CoV-2 BA.2.75 S ectodomain	This study	N/A
Bilirubin	Sigma-Aldrich	Cat# 14370-1G
cOmplete His-Tag Purification Resin	Roche	Cat# 5893682001
Medetomidine hydrochloride (Domitor®)	Nippon Zenyaku Kogyo	N/A
Midazolam	Fujifilm Wako	Cat# 135-13791

(*Continued on next page*)

Please cite this article in press as: Saito et al., Virological characteristics of the SARS-CoV-2 Omicron BA.2.75 variant, Cell Host & Microbe (2022), https://doi.org/10.1016/j.chom.2022.10.003

CellPress
OPEN ACCESS

Continued

REAGENT or RESOURCE	SOURCE	IDENTIFIER
Butorphanol (Vetorphale®)	Meiji Seika Pharma	N/A
Alphaxaone (Alfaxan®)	Jurox	N/A
Isoflurane	Sumitomo Dainippon Pharma	N/A
EnVision FLEX target retrieval solution high pH	Agilent	Cat# K8004
Matrigel growth factor reduced basement membrane matrix	Corning	Cat# 354230
poly-L-lysine	Sigma-Aldrich	Cat# P4832
Remdesivir	Clinisciences	Cat# A17170
EIDD-1931	Cell Signalling Technology	Cat# 81178S
Nirmatrelvir	MedChemExpress	Cat# HY-138687
n-octyl-β-D-glucoside	Dojindo	Cat# O001
Critical commercial assays		
QIAamp viral RNA mini kit	Qiagen	Cat# 52906
NEBNext Ultra RNA Library Prep Kit for Illumina	New England Biolabs	Cat# E7530
MiSeq reagent kit v3	Illumina	Cat# MS-102-3001
One Step TB Green PrimeScript PLUS RT-PCR kit	Takara	Cat# RR096A
SARS-CoV-2 direct detection RT-qPCR kit	Takara	Cat# RC300A
Nano Glo HiBiT lytic detection system	Promega	Cat# N3040
Bright-Glo luciferase assay system	Promega	Cat# E2650
One-Glo luciferase assay system	Promega	Cat# E6130
Cell counting kit-8	Dojindo	Cat# CK04-11
Deposited data		
Viral genome sequencing data of working viral stocks (see also Table S6)	This paper	SRA: PRJDB14324 (https://www.ncbi.nlm.nih.gov/sra)
Cryo-EM map of SARS-CoV-2 BA.2.75 S (closed state 1)	This study	EMD-34221
Cryo-EM map of SARS-CoV-2 BA.2.75 S (closed state 2)	This study	EMD-34222
Cryo-EM map of SARS-CoV-2 BA.2.75 S (1-up state)	This study	EMD-34223
Cryo-EM map of SARS-CoV-2 BA.2.75 S in complex with ACE2	This study	EMD-34224.
Structure of the SARS-CoV-2 BA.2.75 S (close-1 state)	This study	PDB: 8GS6
Experimental models: Cell lines		
Human: HEK293T cells	ATCC	CRL-3216
Human: HEK293 cells	ATCC	CRL-1573
Human: HEK293-ACE2 cells	Motozono et al., 2021	N/A
Human: HEK293-ACE2/TMPRSS2 cells	Motozono et al., 2021	N/A
Human: HEK293S GnTI(-) cells	Reeves et al., 2002	N/A
Human: HOS-ACE2/TMPRSS2 cells	Ferreira et al., 2021; Ozono et al., 2021	N/A
Human: Calu-3/DSP_{1-7} cells	Yamamoto et al., 2020	N/A
African green monkey (*Chlorocebus sabaeus*): Vero cells	JCRB Cell Bank	JCRB0111
African green monkey (*Chlorocebus sabaeus*): VeroE6/TMPRSS2 cells	JCRB Cell Bank	JCRB1819
Yeast (*Saccharomyces cerevisiae*): strain EBY100	ATCC	MYA-4941
Experimental models: Organisms/strains		
Human lung microvascular endothelial cells (HMVEC-L)	Lonza	Cat# CC-2527
Normal human bronchial epithelial cells (NHBE)	Lonza	Cat# CC-2540
Slc:Syrian hamsters (male, 4 weeks old)	Japan SLC Inc.	http://www.jslc.co.jp/pdf/hamster/2020/028_Slc_Syrian.pdf

(*Continued on next page*)

Continued

REAGENT or RESOURCE	SOURCE	IDENTIFIER
Oligonucleotides		
Primers for the construction of plasmids expressing the codon-optimized S proteins of BA.2-bearing variants, see Table S5	This study	N/A
RT-qPCR, forward: AGC CTC TTC TCG TTC CTC ATC AC	Kimura et al., 2022b, 2022c; Meng et al., 2022; Motozono et al., 2021; Saito et al., 2022; Suzuki et al., 2022; Yamasoba et al., 2022b	N/A
RT-qPCR, reverse: CCG CCA TTG CCA GCC ATT C	Kimura et al., 2022b, 2022c; Meng et al., 2022; Motozono et al., 2021; Saito et al., 2022; Suzuki et al., 2022; Yamasoba et al., 2022b	N/A
Primers for the construction of yeast-optimized SARS-CoV-2 BA.2 RBD expression plasmid, see Table S5	This study	N/A
Recombinant DNA		
Plasmid: pCAGGS	Niwa et al., 1991	N/A
Plasmid: psPAX2-IN/HiBiT	Ozono et al., 2020	N/A
Plasmid: pWPI-Luc2	Ozono et al., 2020	N/A
Plasmid: pJYDC1	Addgene	Cat# 162458
Plasmid: pHL-sec	Addgene	Cat# 99845
Plasmid: $pDSP_{1-7}$	Kondo et al., 2011	N/A
Plasmid: $pDSP_{8-11}$	Kondo et al., 2011	N/A
Plasmid: pC-B.1.1 S	Motozono et al., 2021; Ozono et al., 2021	N/A
Plasmid: pC-BA.2 S	Yamasoba et al., 2022b	N/A
Plasmid: pC-BA.4/5 S	Kimura et al., 2022c	N/A
Plasmid: pC-BA.2.75 S	Yamasoba et al., 2022a	N/A
Plasmid: pC-BA.2 K147E S	This study	N/A
Plasmid: pC-BA.2 W152R S	This study	N/A
Plasmid: pC-BA.2 F157L S	This study	N/A
Plasmid: pC-BA.2 K147E/W152R/F157L S	This study	N/A
Plasmid: pC-BA.2 I210V S	This study	N/A
Plasmid: pC-BA.2 G257S S	This study	N/A
Plasmid: pC-BA.2 D339H S	This study	N/A
Plasmid: pC-BA.2 G446S S	This study	N/A
Plasmid: pC-BA.2 N460K S	This study	N/A
Plasmid: pC-BA.2 R439Q S	This study	N/A
Plasmid: pHLsec BA.2.75 S ectodomain	This study	N/A
Plasmid: pHLsec soluble human ACE2	This study	N/A
Software and algorithms		
fastp v0.21.0	Chen et al., 2018	https://github.com/OpenGene/fastp
BWA-MEM v0.7.17	Li and Durbin, 2009	http://bio-bwa.sourceforge.net
SAMtools v1.9	Li et al., 2009	http://www.htslib.org
snpEff v5.0e	Cingolani et al., 2012	http://pcingola.github.io/SnpEff
roblanf/sarscov2phylo: 13-11-20 (GISAID phylogenetic analysis pipeline)	GitHub	https://github.com/roblanf/sarscov2phylo
Minimap2 v2.17	Li, 2018	https://github.com/lh3/minimap2
trimAl v1.2	Capella-Gutiérrez et al., 2009	http://trimal.cgenomics.org

(*Continued on next page*)

Please cite this article in press as: Saito et al., Virological characteristics of the SARS-CoV-2 Omicron BA.2.75 variant, Cell Host & Microbe (2022), https://doi.org/10.1016/j.chom.2022.10.003

Continued

REAGENT or RESOURCE	SOURCE	IDENTIFIER
RAxML v8.2.12	Stamatakis, 2014	https://cme.h-its.org/exelixis/web/software/raxml
CmdStan v2.28.1	The Stan Development Team	https://mc-stan.org
CmdStanr v0.4.0	The Stan Development Team	https://mc-stan.org/cmdstanr/
R v4.1.3	The R Foundation	https://www.r-project.org/
Sequencher v5.1 software	Gene Codes Corporation	N/A
In-house scripts	This study	https://github.com/TheSatoLab/Omicron_BA.2.75
Prism 9 software v9.1.1	GraphPad Software	https://www.graphpad.com/scientific-software/prism/
Fiji software v2.2.0	ImageJ	https://fiji.sc
FlowJo software v10.7.1	BD Biosciences	https://www.flowjo.com/solutions/flowjo
Python v3.7	Python Software Foundation	https://www.python.org
FinePointe Station and Review softwares v2.9.2.12849	DSI	https://www.datasci.com/products/software/finepointe-software
NDP.scan software v3.2.4	Hamamatsu Photonics	https://nanozoomer.hamamatsu.com/jp/en/why_nanozoomer/scan.html
PyMOL v2.1.1 or v2.3.3	Schrödinger	https://pymol.org/2/
CytExpert software v2.4	Beckman Coulter	https://www.beckman.pt/flow-cytometry/research-flow-cytometers/cytoflex/software
ColabFold	Mirdita et al., 2022	https://colab.research.google.com/github/sokrypton/ColabFold/blob/main/AlphaFold2.ipynb#scrollTo=kOblAo-xetgx
MolProbity	Williams et al., 2018	http://molprobity.biochem.duke.edu/
PHENIX v1.20	Adams et al., 2010	http://www.phenix-online.org/
Coot v0.9.6	Emsley and Cowtan, 2004	https://www2.mrc-lmb.cam.ac.uk/personal/pemsley/coot/o
EPU v2.14	Thermo Fisher Scientific	N/A
cryoSPARC v3.3.1	Punjani et al., 2017	https://cryosparc.com/
UCSF Chimera v1.15	Pettersen et al., 2004	https://www.cgl.ucsf.edu/chimera/
UCSF Chimera X v1.1	Goddard et al., 2018	https://www.cgl.ucsf.edu/chimerax/
Other		
Centro XS3 LB960	Berthhold Technologies	N/A
GloMax explorer multimode microplate reader 3500	Promega	N/A
FACS Canto II	BD Biosciences	N/A
GISAID database	Khare et al., 2021	https://www.gisaid.org/
24-well Cell Culture Insert	Falcon	Cat# 353104
96-well black plate	PerkinElmer	Cat# 6005225
3,3'-diaminobenzidine tetrahydrochloride	Dako	Cat# DM827
MAS-GP-coated glass slides	Matsunami Glass	Cat# S9901
A1Rsi Confocal Microscope	Nikon	N/A
QuantStudio 1 Real-Time PCR system	Thermo Fisher Scientific	N/A
QuantStudio 3 Real-Time PCR system	Thermo Fisher Scientific	N/A
QuantStudio 5 Real-Time PCR system	Thermo Fisher Scientific	N/A
StepOne Plus Real-Time PCR system	Thermo Fisher Scientific	N/A
Thermal Cycler Dice Real Time System III	Takara	N/A
CFX Connect Real-Time PCR Detection system	Bio-Rad	N/A
Eco Real-Time PCR System	Illumina	N/A
qTOWER3 G Real-Time System	Analytik Jena	N/A

(*Continued on next page*)

Please cite this article in press as: Saito et al., Virological characteristics of the SARS-CoV-2 Omicron BA.2.75 variant, Cell Host & Microbe (2022), https://doi.org/10.1016/j.chom.2022.10.003

Continued

REAGENT or RESOURCE	SOURCE	IDENTIFIER
7500 Real-Time PCR System	Thermo Fisher Scientific	N/A
CF®640R succinimidyl ester	Biotium	Cat# 92108
96 well plate	Thermo Fisher Scientific	Cat# 268200
CytoFLEX S Flow Cytometer	Beckman Coulter	Cat# N0-V4-B2-Y4
Autostainer Link 48	Dako	N/A
Cell-Culture Treated Multidishes (24-well plate)	Thermo Fisher Scientific	Cat# 142475
Superose 6 Increase 10/300 GL	Cytiva	Cat# 29091596
Buxco Small Animal Whole Body Plethysmography	DSI	https://www.datasci.com/products/buxco-respiratory-products/finepointe-whole-body-plethysmography
MouseOx PLUS	STARR	https://www.starrlifesciences.com/product-category/pulse-oximetry/
Multiskan FC	Thermo Fisher Scientific	N/A
Transwell 6.5mm Polycarbonate Membrane Inserts Pre-Loaded in 24-Well Culture Plates	Corning	Cat# 3413
PDMS (Silicone Elastomer Kit)	Dow Corning	Cat# SYLGARD 184
SU-8 2150	MicroChem	Cat# SU-8 2150
Kai Medical Biopsy Punch 6mm	Kai Corporation	Cat# BP-L60K
Cell Culture Inserts, 3.0-μm pore size inserts, 6-well, Transparent PET	Falcon	Cat# 353091
Quantifoil R2.0/2.0 Cu 300 mesh grid	Quantifoil Micro Tools GmbH	N/A
Vitrobot	Thermo Fisher Scientific	N/A
Krios G4	Thermo Fisher Scientific	N/A
GIF-Biocontinuum energy filter	Gatan	N/A

RESOURCE AVAILABILITY

Lead contact

Further information and requests for resources and reagents should be directed to and will be fulfilled by the lead contact, Kei Sato (keisato@g.ecc.u-tokyo.ac.jp).

Materials availability

All unique reagents generated in this study are listed in the key resources table and available from the lead contact with a completed Materials Transfer Agreement.

Data and code availability

All databases/datasets used in this study are available from the GISAID database (https://www.gisaid.org) and GenBank database (https://www.gisaid.org; EPI_SET ID: EPI_SET_220804hy).

The atomic coordinates and cryo-EM maps for the structures of the BA.2.75 S protein closed state 1 (PDB code: 8GS6, EMDB code: 34221), closed state 2 (EMDB code: 34222), 1-up state (EMDB code: 34223) and in complex with hACE2 (EMDB code: 34224) have been deposited in the Protein Data Bank (www.rcsb.org) and Electron Microscopy Data Bank (www.ebi.ac.uk/emdb/). The computational codes used in the present study and the GISAID supplemental table for EPI_SET ID: EPI_SET_220804hy are available in the GitHub repository (https://github.com/TheSatoLab/Omicron_BA.2.75). Viral genome sequencing data for working viral stocks are available in the Sequence Read Archive (accession ID: PRJDB14324).

Additional Supplemental Items are available from Mendeley Data at https://data.mendeley.com/datasets/nrs6t42wbs [https://doi.org/10.17632/nrs6t42wbs.1]. Any additional information required to reanalyze the data reported in this work paper is available from the lead contact upon request.

EXPERIMENTAL MODEL AND SUBJECT DETAILS

Ethics statement

All experiments with hamsters were performed in accordance with the Science Council of Japan's Guidelines for the Proper Conduct of Animal Experiments. The protocols were approved by the Institutional Animal Care and Use Committee of National University Corporation Hokkaido University (approval ID: 20-0123 and 20-0060). All protocols involving specimens from human subjects recruited

Please cite this article in press as: Saito et al., Virological characteristics of the SARS-CoV-2 Omicron BA.2.75 variant, Cell Host & Microbe (2022), https://doi.org/10.1016/j.chom.2022.10.003

at Kyoto University and Interpark Kuramochi Clinic were reviewed and approved by the Institutional Review Boards of Kyoto University (approval ID: G1309), Chiba University (approval ID: HS202103-03) and Interpark Kuramochi Clinic (approval ID: G2021-004). All human subjects provided written informed consent. All protocols for the use of human specimens were reviewed and approved by the Institutional Review Boards of The Institute of Medical Science, The University of Tokyo (approval IDs: 2021-1-0416 and 2021-18-0617), Kyoto University (approval ID: G0697), Kumamoto University (approval IDs: 2066 and 2074), and University of Miyazaki (approval ID: O-1021).

Human serum collection

Vaccine sera of fifteen individuals who had the BNT162b2 vaccine (Pfizer/BioNTech) (average age: 38 years, range: 24–48 years; 53% male) (Figures 2A–2D) were obtained at one month after the second dose, one month after the third dose, and four months after the third dose. Vaccine sera of fifteen individuals who had the BNT162b2 vaccine (Pfizer/BioNTech) for the first, second, and third doses of vaccination and mRNA-1273 (Moderna) for the fourth dose of vaccination (average age: 42 years, range: 32–56 years; 33% male) (Figure 2D) were obtained at one month after the fourth dose. The details of the vaccine sera are summarized in Table S2.

Convalescent sera were collected from fully vaccinated individuals who had been infected with BA.1 (16 2-dose vaccinated; 10–27 days after testing; average age: 48 years, range: 20–76 years, 44% male) (Figure 2E), fully vaccinated individuals who had been infected with BA.2 (9 2-dose vaccinated and 5 3-dose vaccinated; 11–61 days after testing. n=14 in total; average age: 47 years, range: 24–84 years, 64% male) (Figure 2F), and fully vaccinated individuals who had been infected with BA.5 (2 2-dose vaccinated, 17 3-dose vaccinated and 1 4-dose vaccinated; 10–23 days after testing. n=20 in total; average age: 51 years, range: 25–73 years, 45% male) (Figure 2G). The SARS-CoV-2 variants were identified as previously described (Kimura et al., 2022c; Yamasoba et al., 2022a). Sera were inactivated at 56°C for 30 minutes and stored at –80°C until use. The details of the convalescent sera are summarized in Table S2.

Cell culture

HEK293T cells (a human embryonic kidney cell line; ATCC, CRL-3216), HEK293 cells (a human embryonic kidney cell line; ATCC, CRL-1573) and HOS-ACE2/TMPRSS2 cells (HOS cells stably expressing human ACE2 and TMPRSS2) (Ozono et al., 2021; Ferreira et al., 2021) were maintained in DMEM (high glucose) (Sigma-Aldrich, Cat# 6429-500ML) containing 10% fetal bovine serum (FBS, Sigma-Aldrich Cat# 172012-500ML) and 1% penicillin–streptomycin (PS) (Sigma-Aldrich, Cat# P4333-100ML). HEK293-ACE2 cells (HEK293 cells stably expressing human ACE2) (Motozono et al., 2021) were maintained in DMEM (high glucose) containing 10% FBS, 1 μg/ml puromycin (InvivoGen, Cat# ant-pr-1) and 1% PS. HEK293-ACE2/TMPRSS2 cells (HEK293 cells stably expressing human ACE2 and TMPRSS2) (Motozono et al., 2021) were maintained in DMEM (high glucose) containing 10% FBS, 1 μg/ml puromycin, 200 μg/ml hygromycin (Nacalai Tesque, Cat# 09287-84) and 1% PS. Vero cells [an African green monkey (*Chlorocebus sabaeus*) kidney cell line; JCRB Cell Bank, JCRB0111] were maintained in Eagle's minimum essential medium (EMEM) (Sigma-Aldrich, Cat# M4655-500ML) containing 10% FBS and 1% PS. VeroE6/TMPRSS2 cells (VeroE6 cells stably expressing human TMPRSS2; JCRB Cell Bank, JCRB1819) (Matsuyama et al., 2020) were maintained in DMEM (low glucose) (Wako, Cat# 041-29775) containing 10% FBS, G418 (1 mg/ml; Nacalai Tesque, Cat# G8168-10ML) and 1% PS. Calu-3/DSP_{1-7} cells (Calu-3 cells stably expressing DSP_{1-7}) (Yamamoto et al., 2020) were maintained in EMEM (Wako, Cat# 056-08385) containing 20% FBS and 1% PS. HEK293S GnTI(-) cells (HEK293S cells lacking N-acetylglucosaminyltransferase) (Reeves et al., 2002) were maintained in DMEM (Nacalai Tesque, Cat# 08458-16) containing 2% FBS without PS. Human airway and lung epithelial cells derived from human induced pluripotent stem cells (iPSCs) were manufactured according to established protocols as described below (see "preparation of human airway and lung epithelial cells from human iPSCs" section) and provided by HiLung Inc. AOs and AO-ALI model were generated according to established protocols as described below (see "Airway organoids" and "AO-ALI model" sections).

METHOD DETAILS

Viral genome sequencing

Viral genome sequencing was performed as previously described (Meng et al., 2022; Yamasoba et al., 2022a; Suzuki et al., 2022; Saito et al., 2022; Motozono et al., 2021). Briefly, the virus sequences were verified by viral RNA-sequencing analysis. Viral RNA was extracted using a QIAamp viral RNA mini kit (Qiagen, Cat# 52906). The sequencing library employed for total RNA sequencing was prepared using the NEBNext Ultra RNA Library Prep Kit for Illumina (New England Biolabs, Cat# E7530). Paired-end 76-bp sequencing was performed using a MiSeq system (Illumina) with MiSeq reagent kit v3 (Illumina, Cat# MS-102-3001). Sequencing reads were trimmed using fastp v0.21.0 (Chen et al., 2018) and subsequently mapped to the viral genome sequences of a lineage B isolate (strain Wuhan-Hu-1; GenBank accession number: NC_045512.2) (Matsuyama et al., 2020) using BWA-MEM v0.7.17 (Li and Durbin, 2009). Variant calling, filtering, and annotation were performed using SAMtools v1.9 (Li et al., 2009) and snpEff v5.0e (Cingolani et al., 2012).

Phylogenetic analyses

For construction of an ML tree of Omicron lineages (BA.1–BA.5) sampled from South Africa and BA.2.75 (shown in Figure 1A), the genome sequence data of SARS-CoV-2 and its metadata were downloaded from the GISAID database (https://www.gisaid.org/) (Khare et al., 2021) on July 23, 2022. We excluded the data of viral strains with the following features from the analysis: i) a lack of

Please cite this article in press as: Saito et al., Virological characteristics of the SARS-CoV-2 Omicron BA.2.75 variant, Cell Host & Microbe (2022), https://doi.org/10.1016/j.chom.2022.10.003

collection date information; ii) sampling from animals other than humans, iii) >2% undetermined nucleotide characters, or iv) sampling by quarantine. From each viral lineage, 30 sequences were randomly sampled and used for tree construction, in addition to an outgroup sequence, EPI_ISL_466615, representing the oldest isolate of B.1.1 obtained in the UK. The viral genome sequences were mapped to the reference sequence of Wuhan-Hu-1 (GenBank accession number: NC_045512.2) using Minimap2 v2.17 (Li, 2018) and subsequently converted to a multiple sequence alignment according to the GISAID phylogenetic analysis pipeline (https://github.com/roblanf/sarscov2phylo). The alignment sites corresponding to the 1–265 and 29674–29903 positions in the reference genome were masked (i.e., converted to NNN). Alignment sites at which >50% of sequences contained a gap or undetermined/ambiguous nucleotide were trimmed using trimAl v1.2 (Capella-Gutiérrez et al., 2009). Phylogenetic tree construction was performed via a three-step protocol: i) the first tree was constructed; ii) tips with longer external branches (Z score > 4) were removed from the dataset; iii) and the final tree was constructed. Tree reconstruction was performed by RAxML v8.2.12 (Stamatakis, 2014) under the GTRCAT substitution model. The node support value was calculated by 100 bootstrap analyses.

Modeling the epidemic dynamics of SARS-CoV-2 lineages

To quantify the spread rate of each SARS-CoV-2 lineage in the human population in India, we estimated the relative R_e of each viral lineage according to the epidemic dynamics, calculated on the basis of viral genomic surveillance data. The data were downloaded from the GISAID database (https://www.gisaid.org/) on August 1, 2022. We excluded the data of viral strains with the following features from the analysis: i) a lack of collection date information; ii) sampling in animals other than humans; or iii) sampling by quarantine. We analyzed the datasets of the ten states of India, where $\geq$20 sequences of either BA.2.75 or BA.5 are reported (i.e., Himachal Pradesh, Odisha, Haryana, Rajasthan, and Maharashtra, Gujarat, West Bengal, Delhi, Tamil Nadu, and Telangana). BA.5 sublineages are summarized as "BA.5", and BA.2 sublineages with $\leq$400 sequences are summarized as "other BA.2". Subsequently, the dynamics of the top seven predominant lineages in India were estimated from April 24, 2022, to August 1, 2022, were analyzed. The number of viral sequences of each viral lineage collected each day in each country was counted, and the count matrix was constructed as an input for the statistical model below.

We constructed a Bayesian hierarchical model to represent relative lineage growth dynamics with multinomial logistic regression as described in our previous study (Yamasoba et al., 2022a). In brief, we incorporated a hierarchical structure into the slope parameter over time, which enabled us to estimate the global average relative R_e of each viral lineage in India as well as the average value for each country. Arrays in the model index over one or more indices: L = 7 viral lineages l; S = 10 states s; and T = 100 days t. The model is as follows:

$$\beta_{ls} \sim \text{Student\_t}(6, \beta_l, \sigma_l)$$

$$\mu_{lst} = \alpha_{ls} + \beta_{ls} t$$

$$\theta_{.st} = \text{softmax}(\mu_{.st})$$

$$y_{lst} \sim \text{Multinomial}\left(\sum_l y_{lst}, \theta_{.st}\right)$$

The explanatory variable was time, t, and the outcome variable was y_{lst}, which represented the count of viral lineage l in state s at time t. The slope parameter of lineage l in state s, β_{ls}, was generated from a Student's t distribution with hyperparameters of the mean, β_l, and the standard deviation, σ_l. As the distribution generated β_{ls}, we used a Student's t distribution with six degrees of freedom instead of a normal distribution to reduce the effects of outlier values of β_{ls}. In the model, the linear estimator $\mu_{.st}$, consisting of the intercept $\alpha_{.s}$ and the slope $\beta_{.s}$, was converted to the simplex $\theta_{.st}$, which represented the probability of occurrence of each viral lineage at time t in state s, based on the softmax link function defined as follows:

$$\text{softmax}(x) = \frac{\exp(x)}{\sum_i \exp(x_i)}$$

y_{lst} is generated from $\theta_{.st}$ and the total count of all lineages at time t in state s according to a multinomial distribution.

The relative R_e of each viral lineage in each county (r_{ls}) was calculated according to the slope parameter β_{ls} as follows:

$$r_{ls} = \exp(\gamma \beta_{ls})$$

where γ is the average viral generation time (2.1 days) (http://sonorouschocolate.com/covid19/index.php?title=Estimating_Generation_Time_Of_Omicron). Similarly, the global average relative R_e of each viral lineage was calculated according to the slope hyperparameter β_l as follows:

$$r_l = \exp(\gamma \beta_l)$$

Please cite this article in press as: Saito et al., Virological characteristics of the SARS-CoV-2 Omicron BA.2.75 variant, Cell Host & Microbe (2022), https://doi.org/10.1016/j.chom.2022.10.003

For parameter estimation, the intercept and slope parameters of the BA.2 variant were fixed at 0. Consequently, the relative R_e of BA.2 was fixed at 1, and those of the other lineages were estimated relative to that of BA.2.

Parameter estimation was performed via the MCMC approach implemented in CmdStan v2.28.1 (https://mc-stan.org) with CmdStanr v0.4.0 (https://mc-stan.org/cmdstanr/). Noninformative priors were set for all parameters. Four independent MCMC chains were run with 1,000 and 2,000 steps in the warmup and sampling iterations, respectively. We confirmed that all estimated parameters showed <1.01 R-hat convergence diagnostic values and >200 effective sampling size values, indicating that the MCMC runs were successfully convergent. The above analyses were performed in R v4.1.3 (https://www.r-project.org/). Information on the relative R_e estimated in the present study is summarized in Table S1.

Plasmid construction

Plasmids expressing the codon-optimized SARS-CoV-2 S proteins of B.1.1 (the parental D614G-bearing variant), BA.2 and BA.5 were prepared in our previous studies (Yamasoba et al., 2022a; Suzuki et al., 2022; Saito et al., 2022; Ozono et al., 2021; Kimura et al., 2022a). Plasmids expressing the codon-optimized S proteins of BA.2.75 and BA.2 S-based derivatives were generated by site-directed overlap extension PCR using the primers listed in Table S5. The resulting PCR fragment was digested with KpnI (New England Biolabs, Cat# R0142S) and NotI (New England Biolabs, Cat# R1089S) and inserted into the corresponding site of the pCAGGS vector (Niwa et al., 1991). Nucleotide sequences were determined by DNA sequencing services (Eurofins), and the sequence data were analyzed by Sequencher v5.1 software (Gene Codes Corporation).

To construct plasmids expressing anti-SARS-CoV-2 monoclonal antibodies (adintrevimab, bamlanivimab, bebtelovimab, casirivimab, cilgavimab, etesevimab, imdevimab, regdanvimab, sotrovimab and tixagevimab), we obtained the sequences of the variable regions of these antibodies from the KEGG Drug Database (https://www.genome.jp/kegg/drug/) and The Structural Antibody Database (http://opig.stats.ox.ac.uk/webapps/newsabdab/sabdab/) and artificially synthesized them by Fasmac. The obtained coding sequences of the variable regions of the heavy and light chains were cloned into the pCAGGS vector containing the sequences of human immunoglobulin 1 and kappa constant region (kindly provided by Dr. Hisashi Arase). Plasmids expressing the SARS-CoV-2 spike proteins of the parental D614G (B.1.1), Omicron BA.2 and BA.4/5 were prepared in our previous studies (Yamasoba et al., 2022b; Kimura et al., 2022c; Yamasoba et al., 2022a; Ozono et al., 2021). Plasmids expressing the spike protein of Omicron variants BA.2.75 (GISAID ID: EPI_ISL_13471039) were generated by site-directed overlap extension PCR using pC-SARS2-S BA.2 (Yamasoba et al., 2022a, 2022b) as the template and the primers listed in Table S5. The resulting PCR fragment was subcloned into the KpnI-NotI site of the pCAGGS vector (Niwa et al., 1991) using an In-Fusion® HD cloning kit (Takara, Cat# Z9650N). Nucleotide sequences were determined by DNA sequencing services (Eurofins), and the sequence data were analyzed by Sequencher v5.1 software (Gene Codes Corporation).

Preparation of monoclonal antibodies

Ten monoclonal antibodies (adintrevimab, bamlanivimab, bebtelovimab, casirivimab, cilgavimab, etesevimab, imdevimab, regdanvimab, sotrovimab and tixagevimab) were prepared as previously described (Meng et al., 2022; Yamasoba et al., 2022b; Liu et al., 2021). Briefly, the pCAGGS vectors containing the sequences encoding the immunoglobulin heavy and light chains were cotransfected into HEK293T cells at a 1:1 ratio using PEI Max (Polysciences, Cat# 24765-1). The culture medium was refreshed with DMEM (low glucose) (Wako, Cat# 041-29775) containing 10% FBS without PS. At 72 hours posttransfection, the culture medium was harvested, and the antibodies were purified using an NAb protein A plus spin kit (Thermo Fisher Scientific, Cat# 89948) according to the manufacturer's protocol.

Neutralization assay

Pseudoviruses were prepared as previously described (Yamasoba et al., 2022a, 2022b; Kimura et al., 2022a, 2022c; Motozono et al., 2021; Ferreira et al., 2021; Uriu et al., 2021, 2022). Briefly, lentivirus (HIV-1)-based, luciferase-expressing reporter viruses were pseudotyped with SARS-CoV-2 S proteins. HEK293T cells (1,000,000 cells) were cotransfected with 1 μg psPAX2-IN/HiBiT (Ozono et al., 2020), 1 μg pWPI-Luc2 (Ozono et al., 2020), and 500 ng plasmids expressing parental S or its derivatives using PEI Max (Polysciences, Cat# 24765-1) according to the manufacturer's protocol. Two days posttransfection, the culture supernatants were harvested and centrifuged. The pseudoviruses were stored at –80°C until use.

The neutralization assay (Figures 2 and S2; Tables 1 and S3) was prepared as previously described (Yamasoba et al., 2022a, 2022b; Kimura et al., 2022a, 2022c; Ferreira et al., 2021; Uriu et al., 2021; Uriu et al., 2022). Briefly, the SARS-CoV-2 S pseudoviruses (counting ~20,000 relative light units) were incubated with serially diluted (120-fold to 87,480-fold dilution at the final concentration) heat-inactivated sera or monoclonal antibodies (the concentrations of serially diluted antibodies are indicated in Figure S2) at 37°C for 1 hour. Pseudoviruses without sera were included as controls. Then, a 40 μl mixture of pseudovirus and serum/antibody was added to HOS-ACE2/TMPRSS2 cells (10,000 cells/50 μl) in a 96-well white plate. At 2 d.p.i., the infected cells were lysed with a One-Glo luciferase assay system (Promega, Cat# E6130) or a Bright-Glo luciferase assay system (Promega, Cat# E2650), and the luminescent signal was measured using a GloMax explorer multimode microplate reader 3500 (Promega) or CentroXS3 (Berthhold Technologies). The assay of each serum sample was performed in triplicate, and the 50% neutralization titer (NT_{50}) was calculated using Prism 9 software v9.1.1 (GraphPad Software).

Please cite this article in press as: Saito et al., Virological characteristics of the SARS-CoV-2 Omicron BA.2.75 variant, Cell Host & Microbe (2022), https://doi.org/10.1016/j.chom.2022.10.003

Airway organoids

An airway organoid (AO) model was generated according to our previous report (Sano et al., 2022). Briefly, normal human bronchial epithelial cells (NHBEs, Cat# CC-2540, Lonza) were used to generate AOs. NHBEs were suspended in 10 mg/ml cold Matrigel growth factor reduced basement membrane matrix (Corning, Cat# 354230). Fifty microliters of cell suspension were solidified on prewarmed cell culture-treated multiple dishes (24-well plates; Thermo Fisher Scientific, Cat# 142475) at 37 °C for 10 min, and then, 500 μl of expansion medium was added to each well. AOs were cultured with AO expansion medium for 10 days. For maturation of the AOs, expanded AOs were cultured with AO differentiation medium for 5 days. In experiments evaluating the antiviral drugs (see "Antiviral drug assay using SARS-CoV-2 clinical isolates and AOs" section below), AOs were dissociated into single cells and then were seeded into a 96-well plate.

SARS-CoV-2 preparation and titration

The working virus stocks of SARS-CoV-2 were prepared and titrated as previously described (Meng et al., 2022; Kimura et al., 2022b, 2022c; Yamasoba et al., 2022a; Suzuki et al., 2022; Saito et al., 2022; Motozono et al., 2021). In this study, clinical isolates of B.1.1 (strain TKYE610670; GISAID ID: EPI_ISL_479681) (Suzuki et al., 2022), Delta (B.1.617.2, strain TKYTK1734; GISAID ID: EPI_ISL_2378732) (Saito et al., 2022), BA.2 (strain TY40-385; GISAID ID: EPI_ISL_9595859) (Kimura et al., 2022c) and BA.5 (strain TKYS14631; GISAID ID: EPI_ISL_12812500) (Tamura et al., 2022), and BA.2.75 (strain TY41-716; GISAID ID: EPI_ISL_13969765) were used. In brief, 20 μl of the seed virus was inoculated into VeroE6/TMPRSS2 cells (5,000,000 cells in a T-75 flask). One h.p.i., the culture medium was replaced with DMEM (low glucose) (Wako, Cat# 041-29775) containing 2% FBS and 1% PS. At 3 d.p.i., the culture medium was harvested and centrifuged, and the supernatants were collected as the working virus stock.

The titer of the prepared working virus was measured as the 50% tissue culture infectious dose ($TCID_{50}$). Briefly, one day before infection, VeroE6/TMPRSS2 cells (10,000 cells) were seeded into a 96-well plate. Serially diluted virus stocks were inoculated into the cells and incubated at 37°C for 4 days. The cells were observed under a microscope to judge the CPE appearance. The value of $TCID_{50}$/ml was calculated with the Reed–Muench method (Reed and Muench, 1938).

For verification of the sequences of SARS-CoV-2 working viruses, viral RNA was extracted from the working viruses using a QIAamp viral RNA mini kit (Qiagen, Cat# 52906) and viral genome sequences were analyzed as described above (see "Viral genome sequencing" section). Information on the unexpected substitutions detected is summarized in Table S6, and the raw data are deposited in the GitHub repository (https://github.com/TheSatoLab/Omicron_BA.2.75).

Antiviral drug assay using SARS-CoV-2 clinical isolates and AOs

Antiviral drug assays (Table 2; Figure S3A) were performed as previously described (Meng et al., 2022). Briefly, one day before infection, AOs (10,000 cells) were dissociated, and then seeded into a 96-well plate. The cells were infected with either B.1.1, BA.2, BA.5 or BA.2.75 isolate (100 $TCID_{50}$) at 37 °C for 2 hours. The cells were washed with DMEM and cultured in DMEM supplemented with 10% FCS, 1% PS and serially diluted remdesivir (Clinisciences, Cat# A17170), EIDD-1931 (an active metabolite of molnupiravir; Cell Signaling Technology, Cat# 81178S), or nirmatrelvir (PF-07321332; MedChemExpress, Cat# HY-138687). At 24 hours after infection, the culture supernatants were collected, and viral RNA was quantified using RT–qPCR (see "RT–qPCR" section below). The assay of each compound was performed in quadruplicate, and the 50% effective concentration (EC_{50}) was calculated using Prism 9 software v9.1.1 (GraphPad Software).

Cytotoxicity assay

The cytotoxicity of remdesivir, EIDD-1931 or nirmatrelvir (Figure S3B) was assessed as previously described (Meng et al., 2022). Briefly, one day before the assay, AOs (10,000 cells) were dissociated and then seeded into a 96-well plate. The cells were cultured with the serially diluted antiviral drugs for 24 hours. The Cell Counting Kit-8 (Dojindo, Cat# CK04-11) solution (10 μl) was added to each well, and the cells were incubated at 37 °C for 90 minutes. Absorbance was measured at 450 nm using the a Multiskan FC (Thermo Fisher Scientific). The assay of each compound was performed in quadruplicate, and the 50% cytotoxic concentration (CC_{50}) was calculated using Prism 9 software v9.1.1 (GraphPad Software).

Pseudovirus infection

Pseudovirus infection (Figure 3A) was performed as previously described (Yamasoba et al., 2022a, 2022b; Kimura et al., 2022a, 2022c; Motozono et al., 2021; Ferreira et al., 2021; Uriu et al., 2021, 2022). Briefly, the amount of pseudoviruses prepared was quantified by the HiBiT assay using a Nano Glo HiBiT lytic detection system (Promega, Cat# N3040) as previously described (Ozono et al., 2021, 2020). For measurement of pseudovirus infectivity, the same amount of pseudoviruses (normalized to the HiBiT value, which indicates the amount of HIV-1 p24 antigen) was inoculated into HOS-ACE2/TMPRSS2 cells, HEK293-ACE2 cells or HEK293-ACE2/TMPRSS2 cells and viral infectivity was measured as described above (see "Neutralization assay" section). For analysis of the effect of TMPRSS2 on pseudovirus infectivity (Figure S4A), the fold change of the values of HEK293-ACE2/TMPRSS2 to HEK293-ACE2 was calculated.

Yeast surface display

Yeast surface display (Figure 3B) was performed as previously described (Dejnirattisai et al., 2022; Kimura et al., 2022a, 2022b, 2022c; Yamasoba et al., 2022a; Motozono et al., 2021; Zahradník et al., 2021b). Briefly, the RBD genes ["construct 3" in Zahradník

Please cite this article in press as: Saito et al., Virological characteristics of the SARS-CoV-2 Omicron BA.2.75 variant, Cell Host & Microbe (2022), https://doi.org/10.1016/j.chom.2022.10.003

et al. (2021b), covering residues 330–528] in the pJYDC1 plasmid were cloned by restriction enzyme-free cloning and transformed into the EBY100 Saccharomyces cerevisiae. The primers are listed in Table S5. The expression media 1/9 (Zahradník et al., 2021a) was inoculated (OD 1) by overnight (220 rpm, 30°C, SD-CAA media) grown culture, followed by cultivation for 24 hours at 20°C. The medium was supplemented with 10 mM DMSO solubilized bilirubin (Sigma-Aldrich, Cat# 14370-1G) for expression cocultivation labeling [pJYDC1, eUnaG2 reporter holo-form formation, green/yellow fluorescence (excitation at 498 nm, emission at 527 nm)]. Cells (100 μl aliquots) were collected by centrifugation (3000 g, 3 minutes), washed in ice-cold PBSB buffer (PBS with 1 mg/ml BSA), and resuspended in an analysis solution with a series of CF®640R succinimidyl ester labeled (Biotium, Cat# 92108) ACE2 peptidase domain (residues 18–740) concentrations. The peptidase domain of wild-type ACE2 and ACE2 N90Q were produced and purified as previously described (Zahradník et al., 2021b). The reaction volume was adjusted (1–100 ml) to avoid the ligand depletion effect, and the suspension was incubated overnight in a rotator shaker (10 rpm, 4°C). Incubated samples were washed with PBSB buffer, transferred into a 96-well plate (Thermo Fisher Scientific, Cat# 268200), and analyzed by a CytoFLEX S Flow Cytometer (Beckman Coulter, USA, Cat#. N0-V4-B2-Y4) with the gating strategy described previously (Zahradník et al., 2021b). The eUnaG2 signals were compensated by CytExpert software (Beckman Coulter). The mean binding signal (FL4-A) values of RBD-expressing cells, subtracted by signals of nonexpressing populations, were subjected to the determination of the dissociation constant K_D, Y_D by a noncooperative Hill equation fitted by nonlinear least-squares regression using Python v3.7 fitted together with two additional parameters describing the titration curve (Zahradník et al., 2021b).

Protein expression and purification for cryo-EM

Protein expression and purification were performed as previously described (Hashiguchi et al., 2011). Briefly, the expression plasmid, pHLsec, encoding the BA.2.75 S ectodomain bearing six proline substitutions (F817P, A892P, A899P, A942P, K986P and V987P) (Hsieh et al., 2020) and the deletion of the furin cleavage site (i.e., RRAR to GSAG substitution) with a T4-fold trimerization domain or soluble human ACE2 ectodomain were transfected into HEK293S GnTI(-) cells. The proteins in the culture supernatant were purified with a cOmplete His-Tag Purification Resin (Roche, Cat# 5893682001) affinity column, followed by Superose 6 Increase 10/300 GL size-exclusion chromatography (Cytiva, Cat# 29091596) with calcium- and magnesium-free PBS buffer.

Cryo-EM sample preparation and data collection

For the preparation of a complex sample for cryo-EM, BA.2.75 S ectodomain solution was incubated at 37°C for 1 hour before use. Purified ACE2 was incubated with BA.2.75 S ectodomain at a molar ratio of 1:3.2 at 18°C for 1 hour. A 0.1% (w/v) n-octyl-β-D-glucoside solution (Dojindo, Cat# O001) was added to BA.2.75 S ectodomain solution with or without ACE2 to a final concentration of 0.01%. The sample was then applied to a Quantifoil R2.0/2.0 Cu 300 mesh grid (Quantifoil Micro Tools GmbH), which had been freshly glow-discharged for 120 seconds at 10 mA using PIB-10 (Vacuum Device). The samples were plunged into liquid ethane using a Vitrobot mark IV (Thermo Fisher Scientific) with the following settings: temperature 18°C, humidity 100%, blotting time 5 seconds, and blotting force 5. Micrographs were collected on a Krios G4 system (Thermo Fisher Scientific) operated at 300 kV with a K3 direct electron detector (Gatan) at a nominal magnification of 130,000 (0.67 per physical pixel) using a GIF-Biocontinuum energy filter (Gatan) with a 20-eV slit width. Each micrograph was collected with a total exposure of 1.5 s and a total dose of 50 e/Å2 over 50 frames. A total of 3308 and 3248 micrographs of S and S-ACE2 complexes, respectively, were collected. All micrographs were collected at a nominal defocus range of 0.8–1.8 μm using EPU software v2.14 (Thermo Fisher Scientific).

Cryo-EM image processing

For the BA.2.75 S ectodomain without ACE2, micrograph movie frames were aligned, dose-weighted, and CTF-estimated using Patch Motion correction and Patch CTF in cryoSPARC v3.3.1 (Punjani et al., 2017). A total of 754,589 particles were blob-picked, and reference-free 2D classification (K=150, batch=200, iteration=30) was performed to remove junk particles. Heterogeneous refinement was carried out using the Ab initio model that was reconstructed with 467,029 selected particles after 2D classification in cryoSPARC. The particles belonging to the class of S ectodomains were selected, and five rounds of heterogeneous refinement were performed to isolate the S ectodomain in different conformation states, and each state was selected and processed by nonuniform refinement with CTF refinement in cryoSPARC to generate the final maps. For BA.2.75 S ectodomain with the ACE2 complex, the dataset was preprocessed to 2D classification (K=150, batch=200, iteration=30), in the same way as the BA.2.75 S ectodomain without ACE2, with 682,973 picked particles. A total of 338,745 particles belonging cto lasses that show a representative S ectodomain were selected and subsequently refined against a map of SARS-CoV-2 S in complex with ACE2 (EMDB: EMD-22891) (Xiao et al., 2021) and processed by nonuniform refinement with CTF refinement in cryoSPARC to generate the final maps. The reported global resolutions are based on the gold-standard Fourier shell correlation curve (FSC=0.143) criterion. Local resolutions were calculated with cryoSPARC (Cardone et al., 2013). Workflows of data processing are shown in Figure S4B. Figures related to data processing and final reconstructed maps were prepared with UCSF Chimera v1.15 (Pettersen et al., 2004) and UCSF Chimera X v1.1 (Goddard et al., 2018).

Cryo-EM model building and analysis

The SARS-CoV-2 BA.2 S ectodomain (PDB: 7UB0) (Stalls et al., 2022) was fitted to the corresponding maps using UCSF Chimera v1.15 (Pettersen et al., 2004). Iterative rounds of manual fitting in Coot v0.9.6 (Emsley and Cowtan, 2004) and real-space refinement in Phenix v1.20 (Adams et al., 2010) were carried out to improve nonideal rotamers, bond angles, and Ramachandran outliers. The

Please cite this article in press as: Saito et al., Virological characteristics of the SARS-CoV-2 Omicron BA.2.75 variant, Cell Host & Microbe (2022), https://doi.org/10.1016/j.chom.2022.10.003

final model was validated with MolProbity (Williams et al., 2018). Electrostatic potentials were calculated using APBS Electrostatic plugins (Jurrus et al., 2018) for PyMOL v2.3.3. The structure models shown in the surface, cartoon, and stick presentation in the figures were prepared with PyMOL.

SARS-CoV-2 S-based fusion assay

A SARS-CoV-2 S-based fusion assay (Figures 3G and 3H) was performed as previously described (Kimura et al., 2022b, 2022c; Yamasoba et al., 2022a; Suzuki et al., 2022; Saito et al., 2022; Motozono et al., 2021). Briefly, on day 1, effector cells (i.e., S-expressing cells) and target cells (Calu-3/DSP_{1-7} cells) were prepared at a density of 0.6–0.8 × 10^6 cells in a 6-well plate. On day 2, for the preparation of effector cells, HEK293 cells were cotransfected with the S expression plasmids (400 ng) and $pDSP_{8-11}$ (Kondo et al., 2011) (400 ng) using TransIT-LT1 (Takara, Cat# MIR2300). On day 3 (24 hours posttransfection), 16,000 effector cells were detached and reseeded into a 96-well black plate (PerkinElmer, Cat# 6005225), and target cells were reseeded at a density of 1,000,000 cells/2 ml/well in 6-well plates. On day 4 (48 hours posttransfection), target cells were incubated with EnduRen live cell substrate (Promega, Cat# E6481) for 3 hours and then detached, and 32,000 target cells were added to a 96-well plate with effector cells. *Renilla* luciferase activity was measured at the indicated time points using Centro XS3 LB960 (Berthhold Technologies). For measurement of the surface expression level of the S protein, effector cells were stained with rabbit anti-SARS-CoV-2 S S1/S2 polyclonal antibody (Thermo Fisher Scientific, Cat# PA5-112048, 1:100). Normal rabbit IgG (Southern Biotech, Cat# 0111-01, 1:100) was used as a negative control, and APC-conjugated goat anti-rabbit IgG polyclonal antibody (Jackson ImmunoResearch, Cat# 111-136-144, 1:50) was used as a secondary antibody. The surface expression level of S proteins (Figure 3G) was measured using a FACS Canto II (BD Biosciences) and the data were analyzed using FlowJo software v10.7.1 (BD Biosciences). For calculation of fusion activity, *Renilla* luciferase activity was normalized to the MFI of surface S proteins. The normalized value (i.e., *Renilla* luciferase activity per the surface S MFI) is shown as fusion activity.

Coculture experiment

A coculture experiment (Figure S4D) was performed as previously described (Kimura et al., 2022c; Yamasoba et al., 2022a; Suzuki et al., 2022). This assay utilizes a dual split protein (DSP) encoding *Renilla* luciferase and *GFP* genes; the respective split proteins, DSP_{8-11} and DSP_{1-7}, are expressed in effector and target cells by transfection. Briefly, one day before transfection, effector cells (i.e., S-expressing cells) were seeded on the coverslips coated with poly-L-lysine (Sigma, Cat# P4832) and placed in a 12-well plate, and target cells were prepared at a density of 100,000 cells in a 12-well plate. For preparation of effector cells, HEK293 cells were cotransfected with the S-expression plasmids (500 ng) and $pDSP_{8-11}$ (500 ng) using PEI Max (Polysciences, Cat# 24765-1). For preparation of target cells, HEK293 and HEK293-ACE2/TMPRSS2 cells were transfected with $pDSP_{1-7}$ (500 ng) (Kondo et al., 2011). At 24 hours posttransfection, target cells were detached and cocultured with effector cells in a 1:2 ratio. At 24 h post-coculture, cells were fixed with 4% paraformaldehyde in PBS (Nacalai Tesque, Cat# 09154-85) for 15 minutes at room temperature. Nuclei were stained with Hoechst 33342 (Thermo Fisher Scientific, Cat# H3570). The coverslips were mounted on glass slides using Fluoromount-G (SouthernBiotech, Cat# 0100-01) with Hoechst 33342 and observed using an A1Rsi Confocal Microscope (Nikon). The syncytium size (GFP-positive area) was measured using Fiji software v2.2.0 (ImageJ) as previously described (Kimura et al., 2022c; Yamasoba et al., 2022a; Suzuki et al., 2022).

AO-ALI model

The AO-ALI model (Figure 4D) was generated according to our previous report (Sano et al., 2022). For generation of AO-ALI, expanding AOs were dissociated into single cells, and then were seeded into Transwell inserts (Corning, Cat# 3413) in a 24-well plate. AO-ALI was cultured with AO differentiation medium for 5 days to promote their maturation. AO-ALI was infected with SARS-CoV-2 from the apical side.

Preparation of human airway and lung epithelial cells from human iPSCs

The air-liquid interface culture of airway and lung epithelial cells (Figures 4E and 4F) was differentiated from human iPSC-derived lung progenitor cells as previously described (Kimura et al., 2022c; Tamura et al., 2022; Yamamoto et al., 2017; Konishi et al., 2016; Gotoh et al., 2014). Briefly, lung progenitor cells were induced stepwise from human iPSCs according to a 21-day and 4-step protocol (Yamamoto et al., 2017). At day 21, lung progenitor cells were isolated with the specific surface antigen carboxypeptidase M and seeded onto the upper chamber of a 24-well Cell Culture Insert (Falcon, #353104), followed by 28-day and 7-day differentiation of airway and lung epithelial cells, respectively. Alveolar differentiation medium with dexamethasone (Sigma-Aldrich, Cat# D4902), KGF (PeproTech, Cat# 100-19), 8-Br-cAMP (Biolog, Cat# B007), 3-isobutyl 1-methylxanthine (IBMX) (Fujifilm Wako, Cat# 095-03413), CHIR99021 (Axon Medchem, Cat# 1386), and SB431542 (Fujifilm Wako, Cat# 198-16543) was used for the induction of lung epithelial cells. PneumaCult ALI (STEMCELL Technologies, Cat# ST-05001) with heparin (Nacalai Tesque, Cat# 17513-96) and Y-27632 (LC Laboratories, Cat# Y-5301) hydrocortisone (Sigma-Aldrich, Cat# H0135) was used for induction of airway epithelial cells.

Airway-on-a-chips

Airway-on-a-chips (Figures 4G–4I and S4E) were prepared as previously described (Hashimoto et al., 2022). Human lung microvascular endothelial cells (HMVEC-L) were obtained from Lonza (Cat# CC-2527) and cultured with EGM-2-MV medium (Lonza, Cat# CC-3202). For preparation of the airway-on-a-chip, first, the bottom channel of a polydimethylsiloxane (PDMS) device was precoated

Please cite this article in press as: Saito et al., Virological characteristics of the SARS-CoV-2 Omicron BA.2.75 variant, Cell Host & Microbe (2022), https://doi.org/10.1016/j.chom.2022.10.003

with fibronectin (3 μg/ml, Sigma-Aldrich, Cat# F1141). The microfluidic device was generated according to our previous report (Deguchi et al., 2021). HMVEC-L cells were suspended at 5,000,000 cells/ml in EGM2-MV medium. Then, 10 μl of suspension medium was injected into the fibronectin-coated bottom channel of the PDMS device. Then, the PDMS device was turned upside down and incubated for 1 h. After 1 hour, the device was turned over, and the EGM2-MV medium was added into the bottom channel. After 4 days, AOs were dissociated and seeded into the top channel. AOs were generated according to our previous report (Sano et al., 2022). AOs were dissociated into single cells and then suspended at 5,000,000 cells/ml in the AO differentiation medium. Ten microliter suspension medium was injected into the top channel. After 1 hour, the AO differentiation medium was added to the top channel. In the infection experiments (Figures 4G–4I), the AO differentiation medium containing either B.1.1, Delta, BA.2, BA.5 or BA.2.75 isolate (500 $TCID_{50}$) was inoculated into the top channel (Figure S4E). At 2 h.p.i., the top and bottom channels were washed and cultured with AO differentiation and EGM2-MV medium, respectively. The culture supernatants were collected, and viral RNA was quantified using RT–qPCR (see "RT–qPCR" section above).

Microfluidic device

A microfluidic device was generated according to our previous report (Deguchi et al., 2021). Briefly, the microfluidic device consisted of two layers of microchannels separated by a semipermeable membrane. The microchannel layers were fabricated from PDMS using a soft lithographic method. PDMS prepolymer (Dow Corning, Cat# SYLGARD 184) at a base to curing agent ratio of 10:1 was cast against a mold composed of SU-8 2150 (MicroChem, Cat# SU-8 2150) patterns formed on a silicon wafer. The cross-sectional size of the microchannels was 1 mm in width and 330 μm in height. Access holes were punched through the PDMS using a 6-mm biopsy punch (Kai Corporation, Cat# BP-L60K) to introduce solutions into the microchannels. Two PDMS layers were bonded to a PET membrane containing 3.0-μm pores (Falcon, Cat# 353091) using a thin layer of liquid PDMS prepolymer as the mortar. PDMS prepolymer was spin-coated (4000 rpm for 60 sec) onto a glass slide. Subsequently, both the top and bottom channel layers were placed on the glass slide to transfer the thin layer of PDMS prepolymer onto the embossed PDMS surfaces. The membrane was then placed onto the bottom layer and sandwiched with the top layer. The combined layers were left at room temperature for 1 day to remove air bubbles and then placed in an oven at 60°C overnight to cure the PDMS glue. The PDMS devices were sterilized by placing them under UV light for 1 hour before the cell culture.

SARS-CoV-2 infection

One day before infection, Vero cells (10,000 cells), VeroE6/TMPRSS2 cells (10,000 cells), and HEK293-ACE2/TMPRSS2 cells were seeded into a 96-well plate. SARS-CoV-2 [1,000 $TCID_{50}$ for Vero cells [Figure 4A]; 100 $TCID_{50}$ for VeroE6/TMPRSS2 cells [Figure 4B] and HEK293-ACE2/TMPRSS2 cells [Figure 4C]] was inoculated and incubated at 37°C for 1 hour. The infected cells were washed, and 180 μl of culture medium was added. The culture supernatant (10 μl) was harvested at the indicated timepoints and used for RT–qPCR to quantify the viral RNA copy number (see "RT–qPCR" section below). In the infection experiments using human iPSC-derived airway and lung epithelial cells (Figures 4E and 4F), working viruses were diluted with Opti-MEM (Thermo Fisher Scientific, 11058021). The diluted viruses (1,000 $TCID_{50}$ in 100 μl) were inoculated onto the apical side of the culture and incubated at 37 °C for 1 hour. The inoculated viruses were removed and washed twice with Opti-MEM. For collection of the viruses, 100 μl Opti-MEM was applied onto the apical side of the culture and incubated at 37 °C for 10 minutes. The Opti-MEM was collected and used for RT–qPCR to quantify the viral RNA copy number (see "RT–qPCR" section below). The infection experiments using an airway-on-a-chip system (Figures 4G–4I) were performed as described above (see "Airway-on-a-chips" section).

RT–qPCR

RT–qPCR was performed as previously described (Meng et al., 2022; Kimura et al., 2022b, 2022c; Yamasoba et al., 2022a; Suzuki et al., 2022; Saito et al., 2022; Motozono et al., 2021). Briefly, 5 μl culture supernatant was mixed with 5 μl of 2 × RNA lysis buffer [2% Triton X-100 (Nacalai Tesque, Cat# 35501-15), 50 mM KCl, 100 mM Tris-HCl (pH 7.4), 40% glycerol, 0.8 U/μl recombinant RNase inhibitor (Takara, Cat# 2313B)] and incubated at room temperature for 10 min. RNase-free water (90 μl) was added, and the diluted sample (2.5 μl) was used as the template for real-time RT-PCR performed according to the manufacturer's protocol using One Step TB Green PrimeScript PLUS RT-PCR kit (Takara, Cat# RR096A) and the following primers: Forward *N*, 5'-AGC CTC TTC TCG TTC CTC ATC AC-3'; and Reverse *N*, 5'-CCG CCA TTG CCA GCC ATT C-3'. The viral RNA copy number was standardized with a SARS-CoV-2 direct detection RT-qPCR kit (Takara, Cat# RC300A). Fluorescent signals were acquired using a QuantStudio 1 Real-Time PCR system (Thermo Fisher Scientific), QuantStudio 3 Real-Time PCR system (Thermo Fisher Scientific), QuantStudio 5 Real-Time PCR system (Thermo Fisher Scientific), StepOne Plus Real-Time PCR system (Thermo Fisher Scientific), CFX Connect Real-Time PCR Detection system (Bio-Rad), Eco Real-Time PCR System (Illumina), qTOWER3 G Real-Time System (Analytik Jena) Thermal Cycler Dice Real Time System III (Takara) or 7500 Real-Time PCR System (Thermo Fisher Scientific).

Plaque assay

A plaque assay (Figure 4J) was performed as previously described (Kimura et al., 2022b, 2022c; Yamasoba et al., 2022a; Suzuki et al., 2022). Briefly, one day before infection, VeroE6/TMPRSS2 cells (100,000 cells) were seeded into a 24-well plate and infected with SARS-CoV-2 (0.5, 5, 50 and 500 $TCID_{50}$) at 37°C for 1 hour. Mounting solution containing 3% FBS and 1.5% carboxymethyl cellulose (Wako, Cat# 039-01335) was overlaid, followed by incubation at 37°C. At 3 d.p.i., the culture medium was removed, and the cells were washed with PBS three times and fixed with 4% paraformaldehyde phosphate (Nacalai Tesque, Cat# 09154-85). The fixed cells

Please cite this article in press as: Saito et al., Virological characteristics of the SARS-CoV-2 Omicron BA.2.75 variant, Cell Host & Microbe (2022), https://doi.org/10.1016/j.chom.2022.10.003

were washed with tap water, dried, and stained with staining solution [0.1% methylene blue (Nacalai Tesque, Cat# 22412-14) in water] for 30 minutes. The stained cells were washed with tap water and dried, and the size of plaques was measured using Fiji software v2.2.0 (ImageJ).

Animal experiments

Animal experiments (Figures 5 and S5) were performed as previously described (Kimura et al., 2022b, 2022c; Yamasoba et al., 2022a; Suzuki et al., 2022; Saito et al., 2022; Tamura et al., 2022). Syrian hamsters (male, 4 weeks old) were purchased from Japan SLC Inc. (Shizuoka, Japan). For the virus infection experiments, hamsters were euthanized by intramuscular injection of a mixture of 0.15 mg/kg medetomidine hydrochloride (Domitor®, Nippon Zenyaku Kogyo), 2.0 mg/kg midazolam (Dormicum®, Fujifilm Wako, Cat# 135-13791) and 2.5 mg/kg butorphanol (Vetorphale®, Meiji Seika Pharma) or 0.15 mg/kg medetomidine hydrochloride, 4.0 mg/kg alphaxaone (Alfaxan®, Jurox) and 2.5 mg/kg butorphanol. Delta, BA.2, BA.5 and BA.2.75 (1,000 $TCID_{50}$ or 5,000 $TCID_{50}$ in 100 μl) or saline (100 μl) was intranasally inoculated under anesthesia. Oral swabs were collected at the indicated timepoints for the infection group with a lower inoculum (1,000 $TCID_{50}$ per hamster). Body weight was recorded daily by 7 d.p.i. Enhanced pause (Penh), the ratio of time to peak expiratory follow relative to the total expiratory time (Rpef), and BPM were measured every day until 7 d.p.i. (see below). Subcutaneous oxygen saturation (SpO_2, see below) was monitored at 0, 1, 3, 5, and 7 d.p.i. Lung tissues were anatomically collected at 2 and 5 d.p.i. The viral RNA load in the oral swabs and respiratory tissues was determined by RT–qPCR. These tissues were also used for IHC and histopathological analyses (see below).

Lung function test

Lung function tests (Figure 5A) were routinely performed as previously described (Kimura et al., 2022b, 2022c; Yamasoba et al., 2022a; Suzuki et al., 2022; Saito et al., 2022; Tamura et al., 2022). The three respiratory parameters (Penh, Rpef and BPM) were measured by using a Buxco Small Animal Whole Body Plethysmography system (DSI) according to the manufacturer's instructions. In brief, a hamster was placed in an unrestrained plethysmography chamber and allowed to acclimatize for 30 seconds. Then, data were acquired over a 2.5-minute period by using FinePointe Station and Review software v2.9.2.12849 (DSI). The state of oxygenation was examined by measuring SpO_2 using a mouseOx PLUS pulse oximeter (STARR). SpO_2 was measured for the infection group with a lower inoculum (1,000 $TCID_{50}$ per hamster) by attaching a measuring chip to the neck of hamsters sedated by with 0.25 mg/kg medetomidine hydrochloride.

Immunohistochemistry

Immunohistochemistry (IHC) (Figures 5D and S5A–S5C) was performed as previously described (Kimura et al., 2022b, 2022c; Yamasoba et al., 2022a; Suzuki et al., 2022; Saito et al., 2022; Tamura et al., 2022) using an Autostainer Link 48 (Dako). The deparaffinized sections were exposed to EnVision FLEX target retrieval solution high pH (Agilent, Cat# K8004) for 20 minutes at 97°C for activation, and a mouse anti-SARS-CoV-2 N monoclonal antibody (clone 1035111, R&D Systems, Cat# MAB10474-SP, 1:400) was used as a primary antibody. The sections were sensitized using EnVision FLEX for 15 minutes and visualized by peroxidase-based enzymatic reaction with 3,3'-diaminobenzidine tetrahydrochloride (Dako, Cat# DM827) as substrate for 5 minutes. The N protein positivity (Figures 5D and S5A–S5C) was evaluated by certificated pathologists as previously described (Kimura et al., 2022b, 2022c; Yamasoba et al., 2022a; Suzuki et al., 2022; Saito et al., 2022; Tamura et al., 2022). Images were incorporated as virtual slides by NDP.scan software v3.2.4 (Hamamatsu Photonics). The N-protein positivity was measured as the area using Fiji software v2.2.0 (ImageJ).

H&E staining

H&E staining (Figures 5F and S5D) was performed as previously described (Kimura et al., 2022b, 2022c; Yamasoba et al., 2022a; Suzuki et al., 2022; Saito et al., 2022; Tamura et al., 2022). Briefly, excised animal tissues were fixed with 10% formalin neutral buffer solution and processed for paraffin embedding. The paraffin blocks were sectioned at a thickness of 3 μm and then mounted on MAS-GP-coated glass slides (Matsunami Glass, Cat# S9901). H&E staining was performed according to a standard protocol.

Histopathological scoring

Histopathological scoring (Figure 5G) was performed as previously described (Kimura et al., 2022b, 2022c; Yamasoba et al., 2022a; Suzuki et al., 2022; Saito et al., 2022; Tamura et al., 2022). Pathological features, including (i) bronchitis or bronchiolitis, (ii) hemorrhage with congestive edema, (iii) alveolar damage with epithelial apoptosis and macrophage infiltration, (iv) hyperplasia of type II pneumocytes, and (v) the area of hyperplasia of large type II pneumocytes, were evaluated by certified pathologists, and the degree of these pathological findings was arbitrarily scored using a four-tiered system as 0 (negative), 1 (weak), 2 (moderate), and 3 (severe). The "large type II pneumocytes" are type II pneumocytes with hyperplasia exhibiting more than 10-μm-diameter nuclei. We described "large type II pneumocytes" as one of the notable histopathological features of SARS-CoV-2 infection in our previous studies (Kimura et al., 2022b, 2022c; Yamasoba et al., 2022a; Suzuki et al., 2022; Saito et al., 2022; Tamura et al., 2022). The total histological score is the sum of these five indices.

For measurement of the inflammatory area in the infected lungs (Figures 5H and S5D), four hamsters infected with each virus were sacrificed at 5 d.p.i., and all four right lung lobes, the upper (anterior/cranial), middle, lower (posterior/caudal), and accessory lobes, were sectioned along with their bronchi. The tissue sections were stained by H&E, and the digital microscopic images were

incorporated into virtual slides using NDP.scan software v3.2.4 (Hamamatsu Photonics). The inflammatory area including type II pneumocyte hyperplasia in the infected whole lungs was morphometrically analyzed using Fiji software v2.2.0 (ImageJ).

QUANTIFICATION AND STATISTICAL ANALYSIS

Statistical significance was tested using a two-sided Mann–Whitney *U* test, a two-sided Student's *t* test, a two-sided Welch's *t* test, or a two-sided paired *t*-test unless otherwise noted. The tests above were performed using Prism 9 software v9.1.1 (GraphPad Software).

In the time-course experiments (Figures 3H, 4A–4H, 5A, 5B, and 5G), a multiple regression analysis including experimental conditions (i.e., the types of infected viruses) as explanatory variables and timepoints as qualitative control variables was performed to evaluate the difference between experimental conditions thorough all timepoints. The initial time point was removed from the analysis. The *P* value was calculated by a two-sided Wald test. Subsequently, familywise error rates (FWERs) were calculated by the Holm method. These analyses were performed in R v4.1.2 (https://www.r-project.org/).

In Figures 5D, 5F, and S5, photographs shown are the representative areas of at least two independent experiments by using four hamsters at each timepoint. In Figure S4D, photographs shown are the representatives of >20 fields of view taken for each sample.